Aalto University
School of Chemical
Technology

School of Chemical Technology
Degree Programme of Material Science and Engineering

Stefano Postal

COMPACTION OF TOOL STEELS BY PULSED ELECTRIC CURRENT SINTERING (PECS) PROCESS

Final Project (15 cr) submitted for inspection, Espoo, 7th May, 2014.

Supervisor **Professor Simo-Pekka Hannula**

Instructor **M.Sc.(Tech.) Juho Lotta**
M.Sc.(Tech.) Erkin Cura

Aalto University
School of Chemical
Technology

Aalto University, P.O. BOX 11000, 00076 AALTO

www.aalto.fi

Abstract of Final Project

Author Stefano Postal

Title of final project Compaction of tool steels by pulsed electric current (PECS) sintering process

Department Department of Material Science and Engineering

Professorship Material Science **Code of professorship** MT-45.

Thesis supervisor Prof. Simo-Pekka Hannula

Thesis advisor(s) / Thesis examiner(s) M.Sc.(Tech.) Juho Lotta, M.Sc.(Tech.) Erkin Cura

Date 7.5.2014 **Number of pages** 6+69 **Language** English

Abstract

This study had two major purposes: the microstructural investigation of High Chromium White Iron (HCWI) sintered with Pulsed Electric Current Sintering (PECS) and the evaluation of the abrasion resistance of high chromium white iron mixed with different amounts of Hadfield Steel. The objective was to obtain dense high chromium white iron compacts with fine and uniform carbide and grain structure. The materials included in the study were gas atomized high chromium white iron (2.60 wt% C, 19.48 wt% Cr, 1.02 wt% Nb) and Hadfield steel (1.95 wt% C, 4.09 wt% Cr, 13.87 wt% Mn).

The experimental procedure involved preparation and characterization of the starting powders, consolidation of the powders by pulsed electric current sintering process, and characterization of the resulting compacts. Microstructural studies were carried out to establish a relationship between processing conditions and the resulting microstructure. Abrasion testing was conducted (dry sand rubber wheel test) to investigate the effect of Hadfield additions to the wear performance of the material.

The optimal sintering parameters for obtaining dense high chromium white iron included sintering the material at 1050 °C for 5 minutes, heating rate being 100 °C/min and compaction pressure 50 MPa. The resulting microstructure contained fine chromium carbides dispersed in a martensitic steel matrix. The modification of dwell time and the heating rate did not influence the microstructure to any significant degree. In the abrasion tests the high chromium white iron performed noticeably better (~20% lower weight loss) than the material mixed with Hadfield steel in the abrasion test. The performance of the Hadfield steel was only slightly worse (~7% higher wear loss) than that of the high chromium white iron.

Keywords PECS, High chromium white iron, Hadfield steel, Abrasion resistance

Preface

This final project has been carried out in the Department of Materials Science and Engineering of Aalto University between September 2013 and May 2014. The work concludes my Master's program in Materials Engineering in the University of Trento.
I would firstly like to thank my instructor, Juho Lotta, who patiently guided me through the practical research issues and helped me in the writing of the Thesis. Juho's advices were truly vital through the entire work. I am also thankful to my instructor Erkin Cura for being my mentor in the practical aspects of pulsed electric current sintering.
I would like to thank the supervisor of the Thesis, Professor Simo-Pekka Hannula, for providing me the opportunity to work on this topic and to complete the Thesis in Finland. I am also thankful to my Professor in Italy, Professor Massimo Pellizzari, for being my supervisor and encouraging me along the Thesis work.
I am grateful to all the friends I met during my Erasmus period. They made my stay in Finland an incredible experience, full of unforgettable moments. It is truly incredible of how many things I learned from the people I met all over the Europe. I am also grateful to my friends in Trento as well. They helped me in difficult moments and proved to be the best friends I could ever have hoped for.
I would also like to thank my family for their support throughout my studies. Their support was fundamental. I owe to them most of what I have accomplished in my studies.
Last but not least, I would like to give special thanks to Silvia. There are no words to describe what she means to me and what she has done for me during all these years.

Otaniemi, 7.5.2014

Stefano Postal

Contents

Symbols and abbreviations

Symbols

°C/min	Rate of temperature change
$Fe_{2.7}Mn_{0.3}C$	Chemical formula of iron manganese carbide
G = W(a) – W(fl)	Buoyancy of the submerged solid
M_7C_3	Carbide type, in which M is the metal atom
P_E	Applied pressure
Vs	Fractional solid density
W(a)	Weight of the compact in air
W(fl)	Weight of the compact in liquid
wt%	Mass percent
γ	Surface energy
γ_{sv}	Solid-vapor surface energy
ρ	Density of the compact
ρ(fl)	Density of the liquid
σ	Stress of the surface
dVs/dt	Densification rate

Abbreviations

BSE	Backscattered Electrons
ECAS	Electric Current Activated/Assisted Sintering
EDS	Energy Dispersive X-ray Spectroscopy
HCWI	High Chromium White Iron
HIP	Hot Isostatic Pressing
HP	Hot Pressing
NAPPB	Number of Areas with Prior Particle Boundaries
P/M	Powder Metallurgy
PAS	Plasma Activated Sintering
PECS	Pulsed Electric Current Sintering
SE	Secondary Electrons
SEM	Scanning Electron Microscope
SPS	Spark Plasma Sintering
XRD	X-Ray Diffraction

1 Introduction

High Chromium White Irons (HCWI) are used in industrial applications where high abrasion resistance is required. HCWIs are classified as tool steels and they can be produced using either casting or sintering. The characteristic of this material is the presence of hard alloy carbides that provide excellent abrasion resistance. The abrasion resistance of the material is influenced by the microstructure. The limiting factor for HCWI is the poor toughness that can cause unexpected failure during the service of the components.

Pulsed Electric Current Sintering (PECS) is a technique, which uses pulsed electric current and uniaxial pressure to consolidate powders into bulk. PECS has several advantages, refinement of microstructure being one of the most significant ones.

This thesis investigates the microstructure of High Chromium White Iron sintered with Pulsed Electric Current Sintering technique. Optimization of the sintering parameters was carried out with the aid of microstructural studies. The objective was to obtain dense material with fine and uniform carbides and grain structure. The microstructural studies were carried out to establish a relationship between processing conditions and the resulting microstructure. Investigation of the possibility of mixing HCWI with Hadfield steel in order to improve the toughness of the compacts was carried out. Evaluation of the abrasion resistance of the resulting composite samples was conducted using dry sand rubber wheel test.

The experimental procedure involved preparation and characterization of the powders and the compacts. Mechanical properties of the compacts were investigated by carrying out hardness measurements and fracture surface studies. Dry sand rubber wheel test was used for evaluating the abrasive wear performance of the materials.

2 Wear Resistant Ferrous Alloys

Ferrous alloys are the most commonly used family of materials for structural and tribological applications. The wear resistance of these materials is dependent on the composition, microstructure and wear environment.

The first part of this chapter covers the general aspects of wear resistant ferrous alloys. The second part provides two examples of ferrous materials used in wear resistant applications: High chromium white iron and Hadfield steel.

2.1 Typical Wear Phenomena

Wear is the removal of material from two solid surfaces in contact and in relative motion. Wear mechanisms are usually classified in four categories: abrasive wear, adhesive wear, corrosive wear and fatigue wear [1]. Each class has different mechanisms for removal of the material from the surface but similar factors govern the wear rate. An important parameter that influences wear is the hardness of the material. In the design of a wear resistant material high hardness is a primary requirement since this implies high wear resistance. In case of abrasive wear, besides the hardness, toughness needs to be taken into account as well. In impact type of wear conditions low toughness may result in high wear rates [2]. Therefore each variable that affect the mechanical properties of the material (e.g. composition, processing conditions, and heat treatment) influences the wear resistance as well. In tool steels particularly, wear resistance is dependent on some factors such as matrix type and characteristic of the carbides (e.g. hardness, size, morphology, volume fraction, distribution, orientation) [3, 4].

Besides the material related factors, also the loading condition, the tribological environment, the movement of the contact surface, and the type

of abrasive are important aspects to be taken into account in the study of the wear [5].

2.2 Role of Alloying

Wear resistant ferrous alloys are high-alloy steels, which are usually alloyed with significant amount of carbon and carbide forming elements [6]. These carbides forming elements are transition elements such as chromium, molybdenum, vanadium, and niobium [7, 8]. Transition metal carbides have very high hardness (higher than martensite and cementite) providing high wear resistance [9]. In general, the higher the content of carbide forming alloying elements and the higher the carbon content, the higher the alloy carbide content and hardness of the material.

Besides the composition, wear resistance of ferrous alloys is highly dependent on material processing. Depending on the heat treatment and the presence of appropriate elements, a variety of microstructures with different wear characteristics can be obtained.

In austenitic manganese steels the addition of the alloy elements has a different role. Here manganese is used to modify the diagram phase of the material so that at room temperature austenitic phase is obtained. These alloys possess toughness and high work hardening capacity that provide good wear resistance despite of the low hardness.

2.3 Influence of Microstructure

The wear resistance of a ferrous material is to a large degree determined by its microstructure. As shown in Fig. 1 different phases exhibit different wear resistance. The influence of the matrix on wear resistance is related to the degree of protection offered by the carbides. If the carbides protect the matrix, its role is merely to provide mechanical support. However, if this is not the case and the matrix is preferentially removed by the abrasion

process, then the resistance of the matrix against wear is critical. In this case the carbides may become unsupported and susceptible to spalling and fracture [3]. In the former situation the nature of the matrix does not influence the abrasive wear rate. In the second case there are contradictory studies regards which matrix phase is better between austenite and martensite [10, 4]. In the presence of martensitic matrix, it has been demonstrated that carbides are more resistant to fragmentation than in the presence of austenite. This is because martensite provides better support to the carbides than austenite [10]. Moreover, under condition of repeated impact, martensitic steels have the maximum resistance to spalling. On the other hand, the resistance to crack propagation is greatest in steels with a fully austenitic matrix [11].

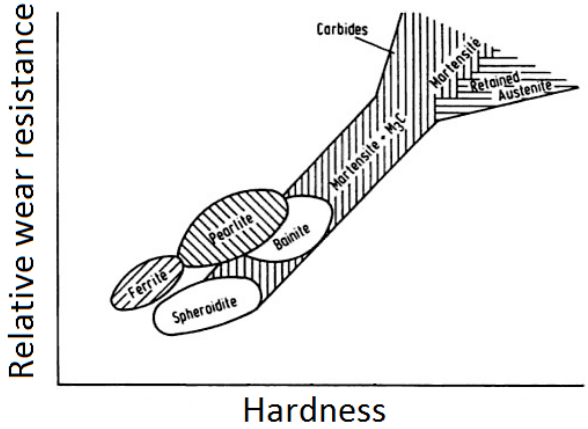

Figure 1: *Relative wear resistance of steels as a function of hardness and microstructure.* [12]

An important parameter to take into consideration is carbide volume fraction since it strongly influences the wear performance of the steels. The influence is very dependent on the wear environment and the wear mechanism. For instance, in case of high chromium white iron abrasive wear resistance increases with increasing carbide volume content up to

about 30 % with a subsequent decrease as carbide volumes increases above 30 % [11].

Another important aspect related to the wear resistance is the size of the carbides. It has been shown that finer and homogeneously distributed carbides improve the wear performance [13, 14, 15]. Refinement of the as-cast structure decreases the mean free path of the matrix and allows greater protection of the matrix by the carbides [3]. A possible method to refine the microstructure is to use powder metallurgical route [16].

The wear resistance depends also on the orientation of the carbides with respect to the wear surface and the wear direction. It has been demonstrated, for instance, that high chromium white irons are more wear resistant when the long axis of the carbides is aligned parallel to the wear surface than when the long axis of the carbides is perpendicular to the wear surface [17, 3].

2.4 Examples of Wear Resistant Ferrous Alloys

2.4.1 High Chromium White Irons

White iron exhibits carbon as cementite or other carbides if it is alloyed with carbide former elements. They have been used for years in applications that require very hard and wear resistance surface but with the disadvantage of low degree of ductility [18]. High Chromium White Irons (HCWI) are a particular subclass of white irons that contain between 11 and 30 wt% of chromium and between 1.8 and 3.6 wt% of carbon [3]. The presence of the chromium changes significantly the equilibrium phase diagram for this material [9], as can be seen in Fig. 2. The commercial HCWIs are used in industrial applications that vary from mining and mineral ore industry [5], cement industry, steel making and ceramic industry. Examples include slurry pumping system, sand handling [19], mineral processing as in mine

drilling, rock machining equipment [3], and components that manipulate and mechanically process aggregates and raw materials [20].

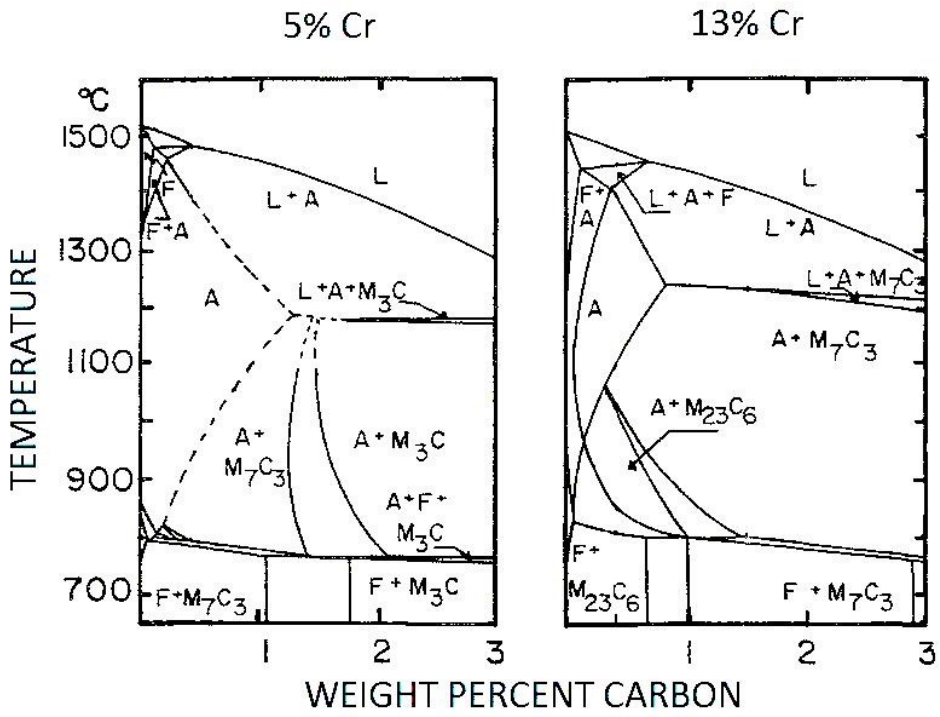

Figure 2: *Vertical section for 5% chromium and 13 % chromium for Fe–C–Cr alloys. A, F and L designate austenite, ferrite and liquid respectively.* [7]

HCWIs are specifically alloyed with chromium because it is a strong carbides former. If the chromium content is greater than 10%, M_7C_3 type of carbide becomes the stable carbon-rich phase of the eutectic reaction [11, 7]. The presence of these carbides has an important role in providing a good wear resistance. Moreover, the presence of chromium helps to prevent the formation of graphite [19] and slightly improves the toughness of the material [13].

The chromium/carbon ratio is of fundamental significance. With a constant amount of chromium, an increase in carbon content improves the wear resistance up to a certain percentage while it results constant with higher amount of carbon [19]. Chromium has in general a strong influence on the

hardenability, but since most of the chromium is in the carbides, its effect is limited in HCWIs. Therefore other alloying elements such as molybdenum, nickel, manganese, and copper are needed to provide adequate hardenability [11, 3]. Molybdenum is the most important element to enhance the hardenability of HCWIs. It suppresses pearlite formation and has little effect on the martensite start temperature. Since molybdenum is expensive [11, 3], other elements such as nickel, manganese, and copper are added to improve hardenability. However, they have less influence than molybdenum and they lower martensite start temperature [3]. Silicon is present in HCWI because it raises martensite start temperature, consequently increasing the amount of martensite attainable [3]. Silicon contents higher than 1 wt%, however, should be avoided because they decrease the hardenability and promote graphitization [11]. Vanadium, tungsten, and niobium, are added to form harder carbides than chromium.

The solidification in the hypoeutectic HCWI occurs by the formation of austenite dendrites followed by the formation of austenite and M_7C_3 chromium carbides [11]. However, when other carbide forming elements are present, the precipitation of these carbides occurs already in the melt. The matrix can be later on extensively modified by heat treatments to obtain for instance a martensitic matrix [3]. The solidification carbide morphology, on the other hand, cannot be efficiently modified later on by heat treatments.

2.4.2 Hadfield Steels

Hadfield steels are a class of steel that contains 11–15 wt% of manganese [21], additional alloying elements including carbon, chromium, nickel, molybdenum, vanadium, titanium, and bismuth. Hadfield steels are low-strength and high-ductility steels [21]. These steels are often used for mineral and mining equipment, grinding and crushing machinery, cement plants, and ore processing [21, 22]. In contrast to HCWIs, they combine high toughness with high work-hardening capacity and good resistance to wear [22, 23]. Their characteristic feature is the tendency to remain

austenitic at room temperature even after slow cooling from high temperatures [21]. As carbon content increases, it becomes difficult to retain the carbon in solid solution. The resulting boundary carbide precipitation is detrimental to both strength and toughness [24]. Nevertheless, because abrasion resistance tends to increase with carbon, carbon content higher than 1.2% may be preferred even though toughness is lowered.

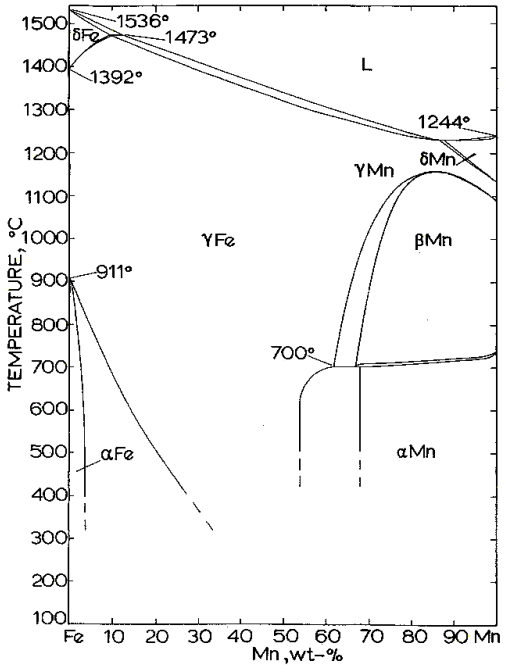

***Figure 3**: Fe–Mn phase equilibrium diagram.* [25]

Another characteristic feature of Hadfield steel is their ability to work-harden. As the work-hardening proceeds, hardness and abrasion resistance of the material increases. At the same time, the interior of the material retains its ductility.

Thus, manganese steels perform best when external conditions cause extensive work hardening of the wear component's surface. If cracking of

the work hardened layer occurs, the crack propagation is quickly inhibited by the tougher core.

Hadfield steels are produced both via casting and powder metallurgy routes. The production of sintered high quality parts in industrial-scale has been a challenge within the past decades [26]. This is related to high oxygen affinity and high vapor pressure of manganese [27].

3 Sintering

Sintering is a thermal treatment to bond particles into a solid structure. It is an optimal choice when there is need for highly reproducible parts and good control over microstructure [28]. Basic steps in powder metallurgy are powder production and powder consolidation. In the latter step the powder is heated to a specific temperature called sintering temperature. At this temperature the particles are bonded together and densification of the material occurs.

3.1 Driving Force of Sintering

The powder initially consists of many particles in contact. The presence of different curvatures is the key of the sintering process. The model sketched in Fig. 4 represents what happens when a curvature is present on a surface.

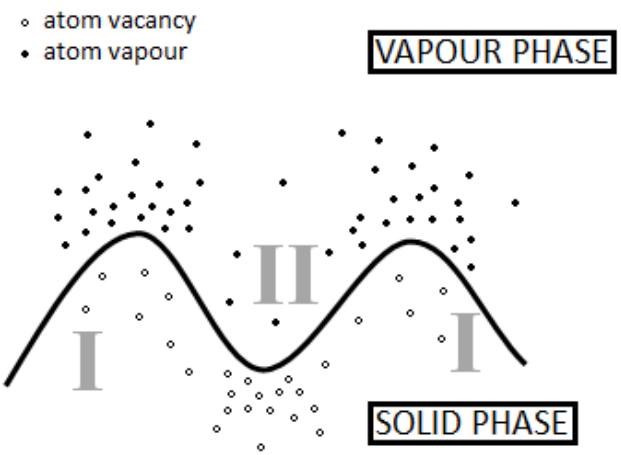

Figure 4: *A schematic drawing showing the distribution of vacancies, and vapour atoms near a curved surface.* [28]

In equilibrium conditions between vapor and solid phase there is a difference in bulk pressure, vapor pressure and in vacancy concentration

between areas with different curvatures. In particular in a concave surface the pressure results higher than in a convex surface. The bulk pressure, which is associated with the curvature, is related to the concept of sintering stress [29]. The stress can be calculated using the surface energy (γ) and the principal radii of curvature of the surface (R1 and R2) as follows:

$$\sigma = \gamma \left(\frac{1}{R1} + \frac{1}{R2}\right) \quad (1)$$

The sintering stress is responsible for the driving force of sintering, because the curved surface has a tendency to flatten to reduce the stress. The stress induces material transport and directs mass flow to give particle bonding [29]. During sintering, the stress is initially responsible for the growth of the neck between the particles and finally for the closure of the pores. The bonding between the particles occurs because this reduces the interfacial area and consequently the free energy of the system. The reduction of total interfacial energy occurs via densification and grain growth [28].

3.2 Sintering Stages and Mechanisms

Sintering can be divided between three main stages, each occurring between a certain material dependent temperature range. The first stage, known as the initial stage, is active at low temperatures. During this stage the neck between the particles grows and the densification starts. The shrinkage, and thus the porosity reduction, does not take place during this stage. The second stage is known as the intermediate stage. In this stage the pores become rounded and elongated. The final stage involves closing of the pores and attainment of the final density [29]. It is important to note that these stages overlap with each other during the heating segment.

The evolution of density is the most straightforward way to investigate the behavior of the material during sintering. Fig. 5 shows an example of the trend of the density plotted against the sintering time and the three sintering stages [28].

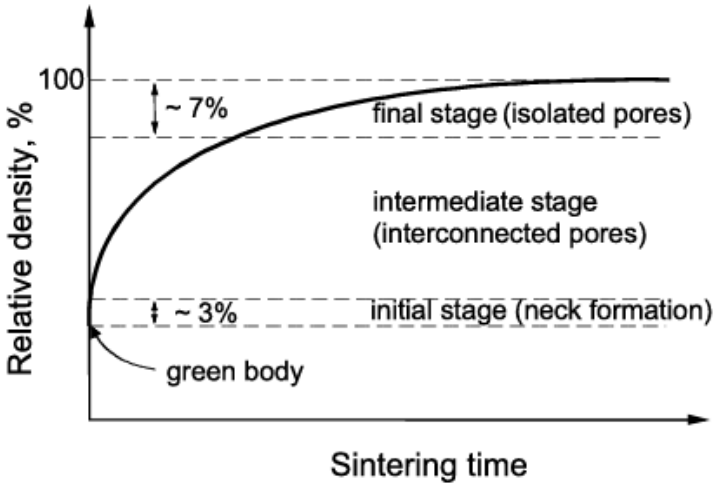

Figure 5: *Typical densification curve of a powder compact and the three sintering stages.* [28]

The sintering mechanisms can be divided in two, surface and bulk transport. Both mechanisms promote neck growth but only the latter one results in shrinkage [29]. The interparticle distance can be reduced only by bulk material flow via viscous flow or material transport from the grain boundary via atom movement. The grain boundaries in particular are an important path for material transport from the point of view of densification and shrinkage [28].

Table 1 lists the classes of sintering mechanisms and the respective material transport mechanisms present during sintering.

***Table 1**: Material transport mechanisms*.

Class of mechanism	Material transport mechanism
Surface mechanism	1. Surface diffusion
	2. Evaporation - condensation
Bulk mechanism	3. Volume diffusion
	4. Grain boundary diffusion
	5. Plastic flow
	6. Viscous flow

In general during sintering more than one mechanism is present at the same time. However, depending on various parameters, such as particles size, neck radius, temperature, and time, there is always one dominant mechanism present [28].

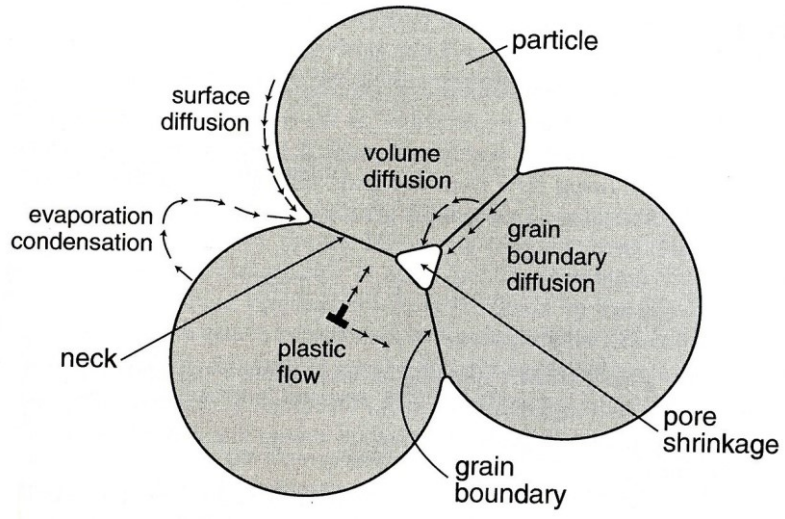

***Figure 6:** A schematic drawing illustrating the possible paths and relatives material transport mechanisms.* [30]

3.3 Sintering Variables

The variables with most influence on densification can be divided in two categories, the ones related to the powder (e.g. chemical composition, particle size, and particle shape) and, those related to the sintering process (e.g. temperature, time, atmosphere, pressure, heating and cooling rate) [28]. Particle size influences the sintering time and temperature. Smaller particle size contributes to higher driving force and thus accelerates the sintering process [28]. Sintering temperature has a strong effect on diffusivity and viscosity [28]. The sintering temperature is typically 0.5–0.8 of the absolute melting temperature of the material [29].Sintering pressure enhances sintering. External pressure enhances densification because it contributes to the sintering stress (i.e. driving force of sintering) [28]. When it is not possible to modify other sintering variables, such as particle size, temperature or time, the application of external pressure can be a valid alternative. One of the most important advantages resulting from the use of external pressure is the elimination of residual porosity [29]. Sintering atmosphere plays an important role in sintering. The shrinkage and consequently the densification reach a maximum when the pressure of entrapped gas becomes equal to the capillarity pressure of the pores. In general, high initial gas pressure and large pores lower the attainable maximum density [28]. Materials that require high sintering temperature, such as tool steels, are usually sintered in vacuum atmosphere [29].

3.4 Sintering of Ferrous Alloys

Iron and steel constitute 85% of the total metal powder production [30]. The types of steel that are formed commonly by sintering include low alloy steels, stainless steels, and tool steels [30]. Sintered ferrous materials have applications that range from aerospace and automotive components to dental components, electrical mechanical systems, and filtration systems [30].

Powder metallurgy is usually at its most competitive against other production routes when the production volume is high and weight of the component ranges from few grams to one kilogram. The shape of the component can be moderately complex, while the size is usually smaller than in cast products [30]. P/M competes with casting, deformation processes, machining, plastic molding, and die casting technologies [30]. It is an effective production route when microstructure control is required in the final product. Disadvantages of powder metallurgy include high cost of raw materials and tools as well as processing complexity [30].

The sintered compact is considered to be fully dense when the porosity is between 0 and 5%. With this level of porosity the mechanical properties are similar to those measured in a material produced with other metal working routes [30]. P/M components typically contain a certain amount of residual porosity and higher density is a precursor to better mechanical properties [30]. Search for novel sintering techniques is therefore a continuous process. Pressure assisted techniques have proven to be superior for removing residual porosity. In the last two decades several novel techniques have been of great interest both in research and industrial use. The key point is that rapid densification occurs when both temperature and pressure are applied simultaneously [30]. Some of the techniques are powder forging, hot pressing uniaxial and isostatic, granular forging, gas forging, hot powder extrusion, and spark plasma sintering.

The sintering mechanism for iron particles is mostly via surface and grain boundary diffusion [30]. Since the atoms diffuse faster in the body-centered cubic crystal structure, sintering requires less time when the temperature is in the range that permits the ferrite to be the stable phase. However, in the austenitic phase the higher temperature permits to regain the sintering rate that is present in the ferrite [30].

As the sintering process proceeds, properties such as strength, ductility, conductivity, magnetic permeability, corrosion resistance, and wear

resistance improve [30]. Different microstructure properties such as porosity, grain size, pore size, and pore shape influence the mechanical properties [30]. With prolonged time at high temperatures a loss in properties can occur. This is known as over-sintering. Full density, however, is not always assurance of good performance. Problems can arise, for instance, due to presence of prior particle boundaries, interfacial contamination or presence of inclusions. In these cases, more attention should be paid on the purity of the powder and the sintering atmosphere [30]. High hardness and good wear resistance are usually the properties with most significance in tool steels [30]. Less emphasis is often put on strength, fatigue resistance, and toughness.

The metal powders used in sintering can be produced by many different methods. Some of the commonly used methods are water or gas atomization, milling, mechanical alloying, electrolysis, and chemical methods. Atomizing has high production rate, wide interval of powder size (from 10 μm up to 1000 μm) and the possibility to use pre-alloyed powders. As a consequence, it is considered the most versatile methods to produce powder in industry [31]. Although several kind of atomization techniques have been developed, the so called two-fluid atomization makes up approximately 95% of the worldwide atomization capacity [31].

Atomization is the breakup of a liquid into fine droplets. In two-fluid atomization techniques the molten metal is broken up by impingement of high pressure jets of different fluids such as water, oil or gas. When gas is used to obtain the powder the process is called gas atomization. Gas atomized powders exhibit high packing density due to spherical shapes. This is often beneficial to the sintering [30].

4 Introduction to Pulsed Electric Current Sintering Technique

Pulsed Electric Current Sintering (PECS) is an advanced sintering technique that uses pulsed DC and uniaxial force to consolidate powders. It is a technique that belongs to the class of Electric Current Activated/Assisted Sintering (ECAS). ECAS is a class of sintering methods that has received in the last 25 years a growing attention because of intrinsic advantages of the method respective to conventional sintering methods and to the observations of the enhanced properties of materials consolidated by this technique. This is confirmed by the number of papers and patent published in the last years. Fig. 7 shows the number of patents from 1900 when the technique was used for the first time.

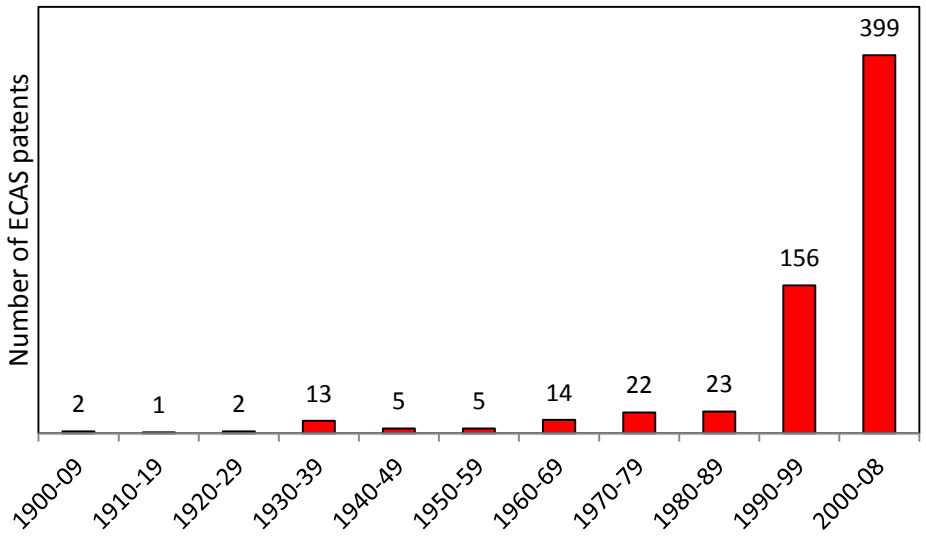

Figure 7: *Number of ECAS patents per decade from 1900 to 2008.* [32]

Fig. 8 shows the exponential increase in the number of papers published on ECAS since1993. The major part of the papers has been published in China with more than 1000 papers between 1994 and 2009. The European country

with the highest number of papers published is France followed by Italy [33].

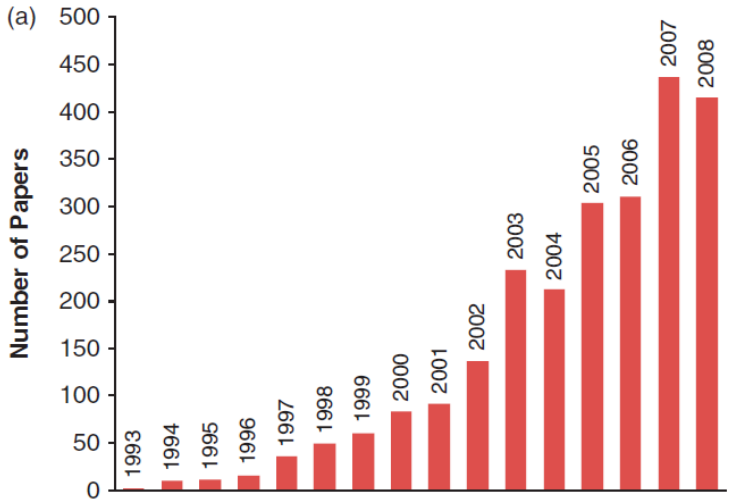

Figure 8: *Number of published paper on ECAS from 1993 to 2008.* [34]

The initial problems presented by PECS technology were related to high cost of equipment [32], problems in industrial scale production [35], poor process control, lack of repeatability, and low sintering efficiency. These factors slowed down the commercialization of the technology [32]. Undoubtedly an important contribution was introduced in 1966 by Inoue who patented electric discharge sintering pioneering PECS method. Although PECS technique has several advantages, various companies started to manufacture PECS machines only when Inoue's patent expired in the late 1980's [32].

Some of the characteristics of the PECS include high sintering rate [35], shorter dwell time, uniform heating [36], and low sintering temperature. Another characteristic include high reproducibility, safety, reliability, economic advantages, and the possibility to process difficult to sinter materials [35]. PECS process is especially well suited for fabrication of

functionally graded materials, intermetallic compounds, fiber reinforced ceramics, metal matrix composites, and nanocrystalline materials. These are all difficult to sinter materials by conventional methods [35].

Confusion can arise because different authors refer to the same process with different names. Some of the most established names include Pulsed Electric Current Sintering (PECS), Spark Plasma Sintering (SPS), Field Assisted Sintering Technique (FAST) and Plasma Activated Sintering (PAS) [37].

4.1 Process Description

PECS system consists of an electrical system that provides current to a mold through two punches. The mold, which holds the powder, is in process chamber where a specific atmosphere can be obtained, usually vacuum. The punches permit the application of a certain pressure on the powder thanks to a mobile piston. Fig. 9 shows a schematic representation of PECS system. The system is controlled by a computer that measures different parameters during the sintering. The most important sintering parameters include temperature, dwell time, heating rate, and pressure. The desired parameter values are communicated to the machine through software prior the compaction. The computer in the PECS executes the program measuring at the same time different values during the sintering. Several types of data, such as the movement of the piston, temperature of the mold, and pressure of the chamber are recorded during the process.

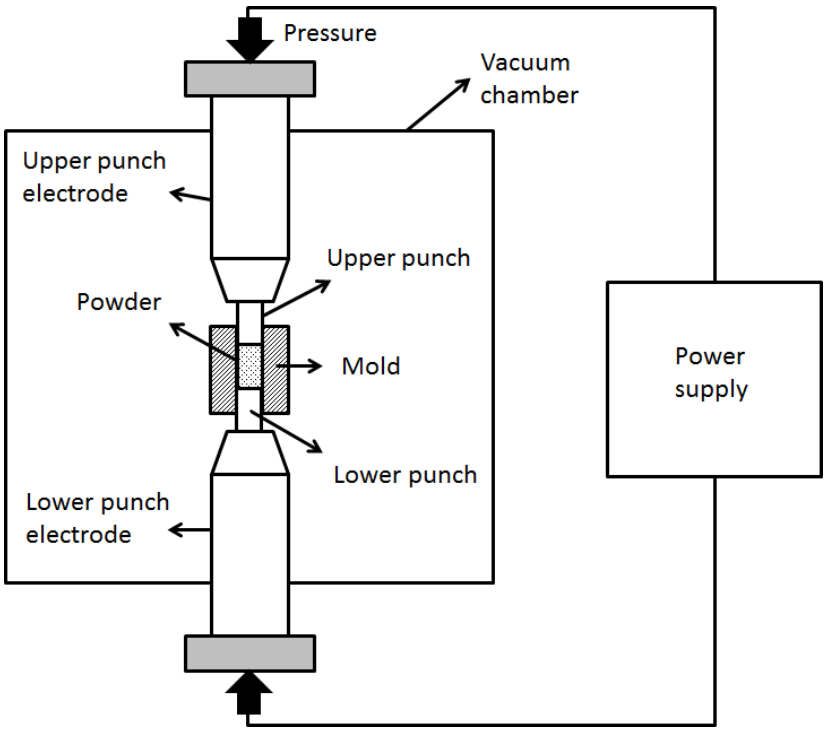

Figure 9: *Schematic of PECS system adapted from* [35].

4.1.1 Heating Rate

PECS enables much higher heating (up to 1000 °C/min) rates than conventional sintering methods. The role of the heating rate on the material can be sometimes critical. For instance, use of high heating rate can minimize the grain growth by minimizing the time spent at temperatures where surface diffusion is promoting rapid grain growth [29]. Experimental evidence of low grain growth has been found in materials sintered with PECS techniques.

High heating rate enhances densification because it shortens the time available for surface diffusion and generates additional driving force by creating large thermal gradients.

4.1.2 Pressure

The densification rate (dV_S/dt) is related to the applied pressure (P_E) by the following formula [29]:

$$\frac{dV_S}{dt} = (1 - V_S)B\left(g\frac{\gamma_{SV}}{x} + P_E\right) \quad (2)$$

in which B is a collection of parameters including diffusivity, temperature, and particle size, g represents a geometric term, V_s is the fractional solid density, x is the scale of the microstructure and γ_{sv} is solid-vapor surface energy.

The application of pressure during sintering has the initial effect on rearrangement of the particles and its importance depends on the particle size of the powder [38]. In PECS the maximum pressure is limited by the low mechanical strength of the graphite, the theoretical upper limit for its compressive strength being about 140 MPa [33].

Fig. 10 shows the effect pressure has on zirconia when sintered using PECS. It is possible to obtain the same density with higher pressure at a lower temperature. This is beneficial when one is aiming for smaller grain size.

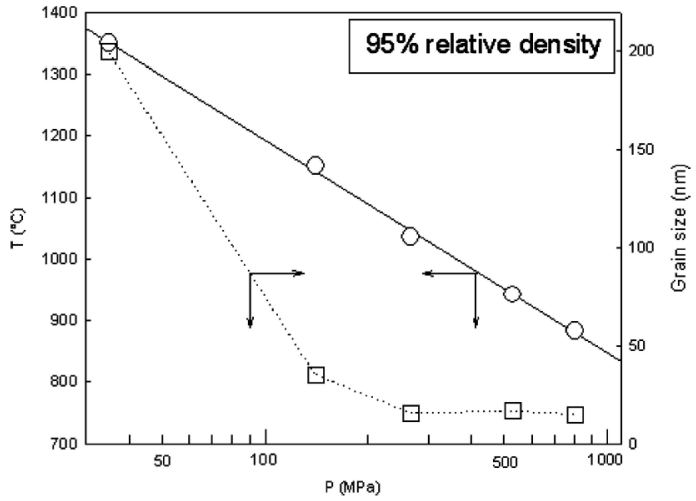

Figure 10: *Effect of pressure on the temperature needed to achieve 95% relative density for cubic ZrO_2. The graph also shows the corresponding decrease in grain size.* [38]

4.1.3 Role of the Current

In PECS process the heat is generated by electric current running through the graphite mold (and the material if its conductivity is high enough) due to graphite's resistance. This phenomenon is known as Joule heating. If the powder is conductive the current passes directly through the powder, whereas if it is not conductive, only the mold is heated by the Joule effect [39]. The main function of the current is to heat up the powder to the sintering temperature. The other effects generated by the pulsed current include:

- Electric field,
- Magnetic field,
- Electrical diffusion field effect.

Fig. 11 illustrates the flow of the current through the powder particles inside the die.

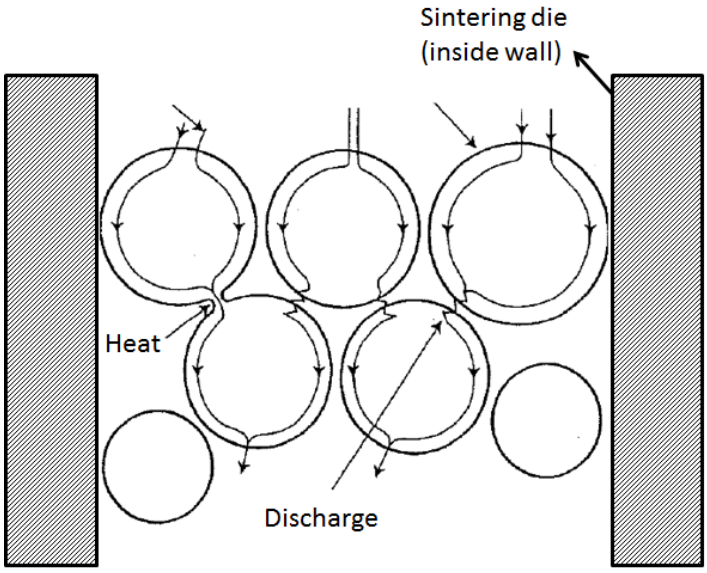

Figure 11: *Current flow through powder particles (adapted from* [35]*).*

The temperature at the neck is much higher than inside the particles because the electrical density of the current flowing through the neck is higher. This promotes quick neck growth and consequently faster sintering [40].

The effect of an electrical field has been shown also on several processes that imply atom movement (phase transformation, nucleation, and growth, etc.) such as crystal defect motion, crystal nucleation and growth, evaporation, and oxidation processes [36]. In sintering process, the influence of the current on mass transport is beneficial densification as it promotes atom movement. The neck formation (initial stage) in fact shows an increase in growth kinetic while a current is applied [33]. On the contrary, there is no direct evidence of the effect of the current in the intermediate and final stages of sintering, but it is proved that the electric field enhances mass transport and thus it is beneficial during all sintering stages [33]. The direction of the current and the pulse pattern have not been shown to have any effect on kinetics of mass transport [36]. The same is true for the frequency of the pulsating current [38].

The presence of rapid joule heating effect and the enhanced mass transport due to the current are well established mechanisms. These two mechanisms contribute to explain the enhanced sintering in PECS process [41]. Another mechanism proposed is the presence of plasma between the particles. Some authors state that spark discharge appears in gaps or at the contact points of the particles. This produces momentarily a high temperature-state of around 10000 °C, resulting in evaporation and melting on the particle surfaces [35]. One of the reasons for enhanced sintering in PECS is thought to be the generation of spark plasma that eliminates adsorptive gas and impurities existing on the surface of the particles [35]. Nevertheless, recent investigation on this phenomenon excludes the presence of plasma. Besides the experimental evidence, the presence of plasma is unlikely, considering that discharge is not possible in non-conductive material and that when the particle contacts increase (due to sintering or applied pressure) results difficult to generate spark discharge [33]. As a consequence the role of the pulsed current remains not completely understood [36].

It is important to take into account that besides all the advantages of PECS technique, it is difficult to obtain homogeneous temperature distribution. This is due to the fact that current and consequent temperature distribution is sensitive to the homogeneity of density distribution [39]. Thus the gradient of the temperature in the sample could cause a possible inhomogeneity in the density of the sample. That is the reason why most of the specimens sintered so far have simple shape. In general, the better the heat conductivity of the material, the smaller the temperature difference [40].

5 Experimental Procedures

PECS was used for sintering of HCWI powder into compacts. Materials characterization was carried out in order to establish a relationship between the processing conditions and material properties. Composite samples with different amounts of HCWI and Hadfield Steel powder were sintered as well. Their microstructure was characterized and abrasion resistance tested.

This chapter describes the procedures of powder preparation, pulsed electric current sintering, materials characterization for HCWI, Hadfield Steel, and the composite samples.

5.1 Starting Materials

The HCWI powder was produced by gas atomization as a by-product of a spray forming experiment at the University of Bremen. Table 2 lists the atomization parameters.

Table 2: *Gas atomization parameters*

Temperature of the melt	1441 °C
Superheat	150 °C
Melt nozzle diameter	5.0 mm
Atomization pressure	4.0 bar
Gas mass flow	0.275 Kg/s
Melt mass flow	0.272 Kg/s

Table 3 lists the chemical composition of the starting material used for the spray forming experiment.

***Table 3**: Chemical composition of the starting material for the spray forming experiment (wt%) (balanced by Fe).*

C	Cr	Nb	Si	Mn	Ni	Mo	V	P	S	Fe
2.42	21.3	1.04	1.16	0.81	0.32	0.81	0.1	0.03	<0.01	Bal.

The Hadfield steel powder was produced by Osprey Ltd. Both powders were sieved before any other action with a Retsch ISO 3310-1 sieve with mesh size of 63 μm. The chemical composition of the powders was determined by ICP-OES (Cr, Fe, Mn, Mo, and Ni) technique by Labtium Oy (carbon content was analyzed pyrolitically). In case of the Hadfield steel, the elements not included in the analyses were determined by EDS. EDS was used for Hadfield steel to determine the concentrations of the missing elements. In case of the HCWI, the concentrations of the missing elements were supplemented with the values presented in Table 3.

Mixing of the Powders

The powder mixtures for making of HCWI–Hadfield Steel composites were produced using Turbula shaker (Willy A. Bachofen AG maschinenfabrik T2C) for 2 hours. A total of five different compositions were prepared. Table 4 lists the sample IDs and respective weight percentages of HCWI.

***Table 4**: Weight percentage of HCWI in the composite samples (set D)*

Sample ID	HCWI percentage (wt%)
D0	0
D25	25
D50	50
D75	75
D100	100

5.2 Characterization of the Powders

5.2.1 Particle Size Distributions

Particle size distributions were measured by laser diffraction with a laser particle size analyzer (Beckman Coulter LS 230).

5.2.2 Microstructure and Particle Morphology

Microstructure and particle morphology of the powders was examined with a Scanning Electron Microscope (SEM), LEO 1450 by LEO Electron Microscopy Ltd.

In order to analyze the microstructure with SEM, it was necessary to mount the powder in epoxy. The samples were ground with SiC-papers (P120, P240, P400, and P1200) and polished with diamond paste (6 μm, 3 μm, and 1 μm). After polishing the samples were etched: HCWI was etched with Aqua Regia (18 ml HCl, 6 ml HNO_3, and 20 ml H_2O) and Hadfield Steel with Nital (10%).

To study particle morphology, small amount of powder was placed on a double sided carbon tape, which was then observed with SEM.

5.2.3 Phase Composition

Phase composition of the powders was determined by X-ray diffraction (XRD). The instrument used was PANanalytical X'pert powder x-ray diffraction platform. The measurements were performed on HCWI and Hadfield Steel powders with the following parameters: step size 0.013, 59.9 second collection time per step, angular range 15–100°, divergent slit 0.5, antiscatter slit 1°, Pixcel slit with monochromator 6.4, 40 KV and 45 mA. The XRD data was analyzed using X'pert high score plus software.

5.3 Current Electric Current Sintering Procedure

Sintering of the powders was performed in a pulsed electric current sintering furnace (FCT HP D25-2, FCT Systeme GmbH), shown in Fig. 12. This machine is capable of sintering samples with a maximum diameter of 80 mm, using a maximum pressing force of 250 kN, maximum voltage and currents of 8 V and 8 kA, and a maximum heating power of 60 kVA [42].

The PECS furnace consists of a control and process units. The latter one includes the process chamber. From the control unit is possible to start, stop and follow the sintering parameters during the process, as well as operate the process chamber.

Figure 12: *The pulsed electric current sintering furnace (FCT HP D 25-2) at Aalto University.*

5.3.1 Sintering Cycle

The sintering cycles, which are constructed using a computer software, consist of several segments, each one corresponding to a specific stage in

the sintering process. The segment sequence is usually as follows: vacuum, pressing, heating, dwell, and cooling segment.

At the beginning of the process, a vacuum is pumped inside the process chamber. During the heating segment the temperature increases as electric current passes through the mold. The temperature can be measured either with thermocouples or pyrometer. The pyrometer measures the temperature (only above 450 °C) from a cavity in the upper punch, approximately 5 mm above the upper surface of the sample. The end of the heating segment is typically followed by dwell segment, which is followed by cooling segment.

5.3.2 Preparation of the Mold

Preparation of the graphite mold, carried out just prior to sintering, includes preparation of the graphite foils, assembling of the mold, and pouring the powder inside the mold. The mold consists of a hollow cylinder body and two punches. These are shown in Fig. 13a.

To protect the mold from the contact with the powder, the interior of the body part is first covered with graphite foil. The lower punch is then inserted into the body. Another graphite foil is placed to protect the surface of the punch. The powder is poured into the mold and the upper punch and the respective graphite foil are used to close the mold. When the mold is ready, an insulating felt is wrapped around it to minimize heat dissipation from the mold to the surrounding.

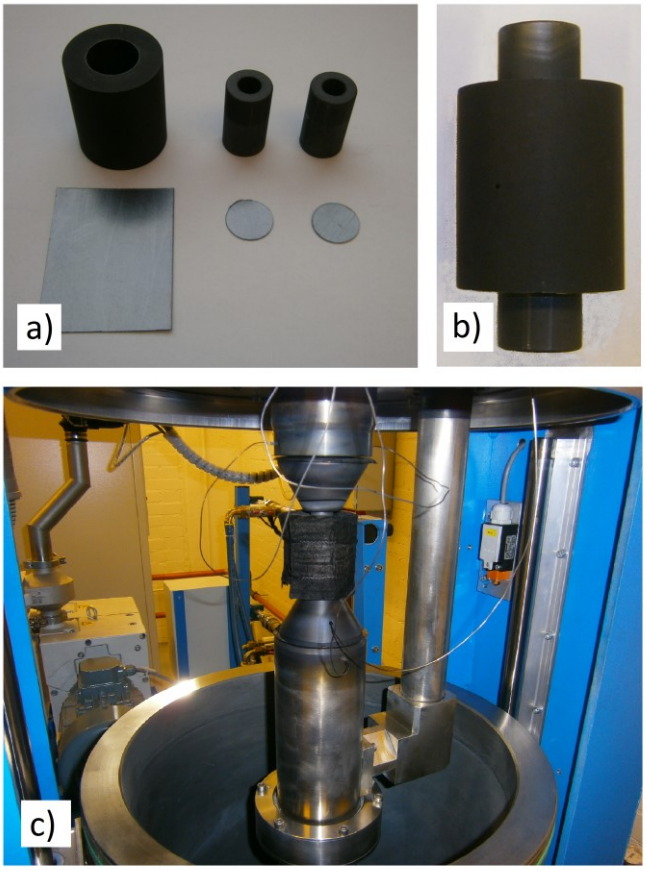

Figure 13: *a) The graphite mold before assembly: The hollow body, the punches, and the pieces of graphite foils protecting the interior of the mold). b) The assembled mold. c) The assembled mold placed between graphite cones and electrodes inside the process chamber of the PECS equipment.*

The assembled mold is placed inside the PECS chamber between two cones that are in contact with the electrodes/pistons, as illustrated in Fig. 13c. Two mold types of different dimensions were used in this work. The smaller mold type was for sintering of samples with a diameter of 20 mm, while the larger one was for sintering of samples with a diameter of 40 mm. The amount of powder was 10 g for the ø20 mm samples and 60 g for ø40 mm samples.

5.3.3 Sintering of High Chromium White Iron

In order to study the sintering behavior of the HCWI, the compactions were divided into three sets. Each set focused on changing one parameter (e.g. heating rate). Table 5 lists the sample IDs and the values of the respective parameters.

Sintering temperature was the only process variable that was changed in Set A. Different values were used to study the densification behavior and to determine the maximum temperature suitable for the sintering of the material. In set B, three different dwell times were used. The aim was to evaluate the relationship between the dwell time and microstructure. In set C, all the process variables apart from heating rate were kept constant to investigate its influence on microstructure.

Two test compactions were additionally carried out in attempt to remove prior particle boundaries found on the surface of the samples (see chapter 6.3). The first compaction used very slow heating rate of 10 °C/min between 850 °C to 1050 °C. The second compaction involved maintaining the temperature at 500 °C for 10 minutes during the heating to sintering temperature. This was thought to minimize the amount of prior particle boundaries by promoting removal of gas originating from compounds decomposing at relatively low temperatures.

Table 5: *Samples IDs and the process parameters for the HCWI samples.*

No.	Set	Process parameters
1	A	100 °C/min, 900 °C, 0 min
2		100 °C/min, 950 °C, 0 min
3		100 °C/min, 1000 °C, 0 min
4		100 °C/min, 1050 °C, 0 min
5		100 °C/min, 1100 °C, 0 min
1	B	100 °C/min, 1050 °C, 5 min
2		100 °C/min, 1050 °C, 10 min
3		100 °C/min, 1050 °C, 20 min
1	C	25 °C/min, 1050 °C, 5 min
2		400 °C/min, 1050 °C, 5 min

5.3.4 Sintering of Hadfield Steel

The evaluation of Hadfield steel's sintering behavior focused on sintering temperature. A test compaction was carried out at 1050 °C for 5 minutes using a heating rate of 100 °C/min.

5.3.5 Sintering of the Composites

The powder mixtures were sintered using the same set of processing parameters. The temperature was set to 1040 °C, the dwell time to 3 minutes, and heating rate to 100 °C/min. A sample with a diameter of 20 mm was first made in order to evaluate the mixing quality between the components. Another 5 samples with a diameter of 40 mm were then compacted to be used in abrasion testing.

5.4 Characterization of the Compacts

The graphite foil covering the samples was removed by sandblasting. Further sample preparation steps included grinding with SiC papers (P120, P240, P400, and P1200) and polishing with diamond paste (6 μm, 3 μm, 1 μm). After polishing, most of the samples were treated either with Nital or water diluted Aqua Regia to reveal their microstructure.

5.4.1 Density

Densities were measured by Archimedes' method using Sartorius Analytical Balance CPA224S. The following equation was used to calculate the density of a sample:

$$\rho = \frac{W(a) \times [\rho(fl) - 0.012\ g/cm^3]}{0.99983\ G} + 0.0012\ g/cm^3 \qquad (3)$$

where ρ is the density of the sample, W(a) is the weight of the sample in air, ρ(fl) is the density of the liquid, W(fl) is the weight of the sample in liquid and G = W(a) – W(fl) is the buoyancy of the submerged solid [43].

For the samples with high level of porosity, a thin layer of beeswax was applied on the surface to seal the pores. The effect of the wax on the weight of the sample was determined to be negligible.

5.4.2 Phase Composition

Determination of phase composition was carried out by XRD as described in chapter 5.2.3.

5.4.3 Microstructure

Microstructure of the samples was studied by optical microscope and scanning electron microscope with a field emission gun (FE-SEM, Hitachi S-4700). During SEM work, the microstructure was studied both with, secondary electrons (SE) – for grain structure and morphology – and backscattered electrons (BSE) – for revealing carbide formation and porosity. Prior to SEM, the samples were coated with carbon (Leica EM SCD050) to enhance the electrical conductivity and improve the quality of the images.

The evaluation of the porosity was done by employing image analysis program (ImageJ) from BSE images (BSE, Back Scattered Electrons). Ten images from different areas of the samples were captured and analyzed. The evaluation of the porosity was carried out only for the samples in set A.

In order to study residual porosity, the fracture surface of some of the samples was observed with SEM (Hitachi S-4700) in SE-mode. The fracture surfaces were produced by breaking ø20 mm samples with the aid of a hydraulic press.

5.4.4 Chemical Composition

The Energy Dispersive Spectroscopy (EDS) analysis was carried out with an energy dispersive spectrometer (Oxford Instruments INCA) equipped on SEM (LEO 1450). EDS was used to evaluate the concentration gradients in the composite samples and presence of quartz sand in the samples after the abrasion test.

5.4.5 Hardness

Hardness measurements were carried out by Struers DuraJet bench-top hardness tester according to EN ISO 6508. The reported Rockwell-C hardness values are averages of five measurements.

5.5 Abrasion Testing

Abrasion testing was carried out using rubber wheel abrasion test, shown in Fig. 14 [44]. The test involves pressing a specimen against a rotating rubber wheel, while sand is fed into the gap between the wheel and specimen. The test used silica sand with a nominal particle size ranging from 100 μm to 600 μm. During the test, the sand flow rate was ~190 g/min, the applied load was ~61 N and the test was carried for 15 minutes with 5 minutes intervals (total wear distance: ~2381 m). The samples were weighted before testing and after each 5 minutes interval.

The test was conducted using ø40mm samples with polished (with 1 μm diamond) surfaces of interest. In order to fit the samples to the sample holder, the samples were cut to a width of 25.5 mm, as illustrated in Fig. 15.

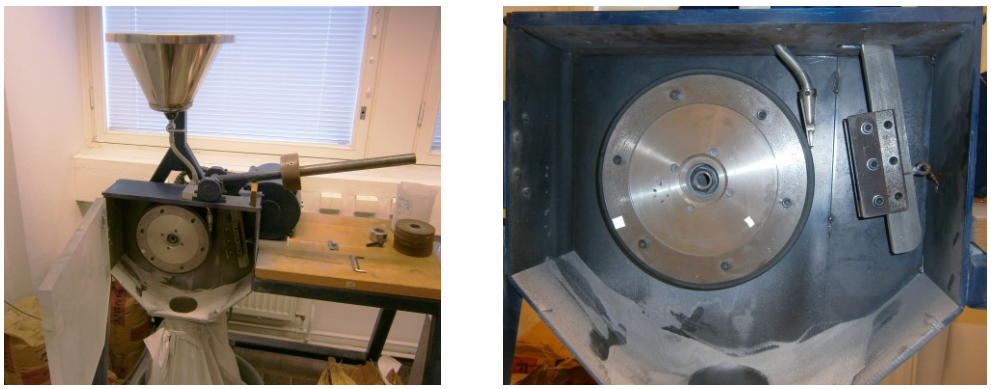

***Figure 14**: Rubber wheel abrasion test setup in Aalto University.*

An auxiliary metal piece was applied due to the short length of the samples to ensure proper sand flow. Fig.15 shows a schematic drawing of the cut sample, the auxiliary piece, and the respective dimensions.

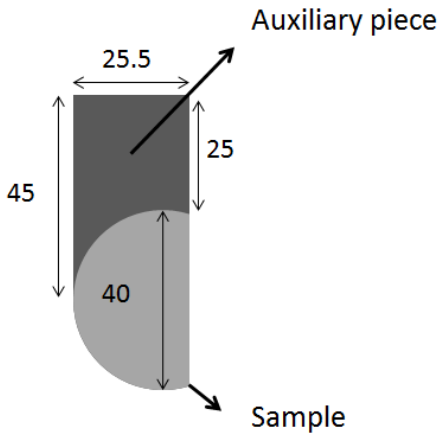

Figure 15: *A schematic drawing of the cut sample fit into the auxiliary piece (dimensions in millimeters).*

6 Results

6.1 Properties of the Powders

The chemical compositions of the HCWI and Hadfield steel are listed in table 6.

Table 6: *Chemical composition (wt%) of the powders (balanced by Fe).*

Alloy	Cr	Si	Nb	Mn	Mo	Ni	V	C
HCWI	19.48	1.13	1.02	0.71	0.68	0.31	0.10	2.60
Hadfield steel	4.09	0.73	-	13.87	0.10	0.44	0.49	1.95

Figs. 16 and 17 show the XRD curves of the HCWI and Hadfield Steel powders. The HCWI powder appeared to consist of austenite, M_7C_3-type of carbides (M = Cr, Fe), and martensite.

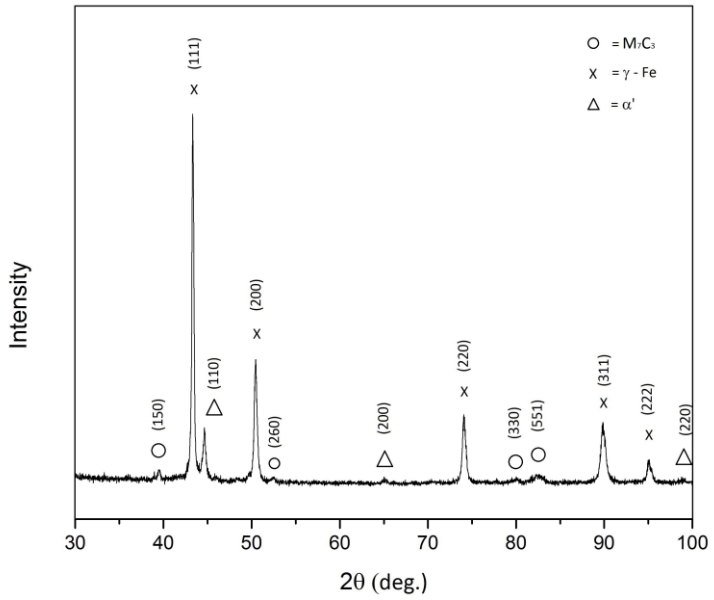

Figure 16: *X-ray curve illustrating the phase composition of the HCWI powder.*

The XRD curve obtained from the Hadfield Steel powder, shown in Fig. 17, indicated that the material consisted of austenite.

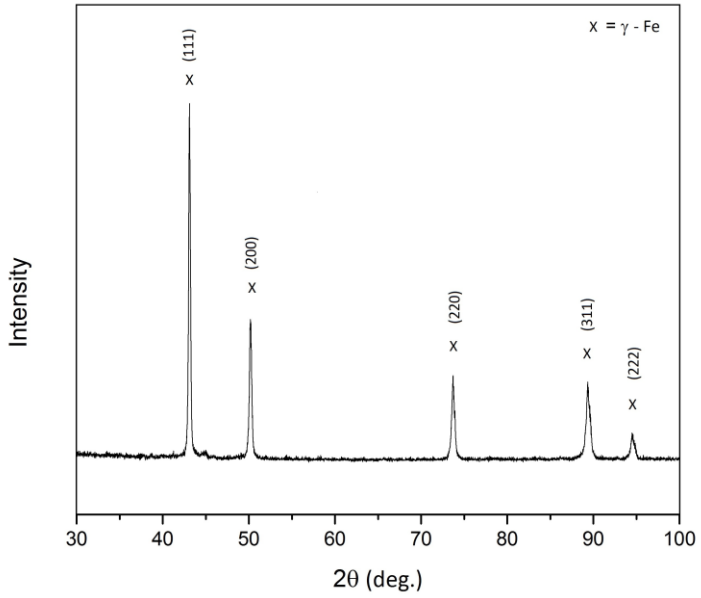

Figure 17: *X-ray curves illustrating the phase composition of the Hadfield steel powder*

Fig. 18a shows the particle size distribution of the HCWI powder. The particle size distribution was positively skewed and bimodal. The mean particle diameter was 37.10 μm. The positive skew indicated the presence of considerable amount of large particles. The bimodal nature of the particle size distribution confirmed that both small and large particles were present. The larger particles were believed to be elongated particles that passed through the sieve grid.

Fig. 18b illustrates particle morphology in the HCWI powder. Although some elongated particles were present, most of the particles were fairly spherical.

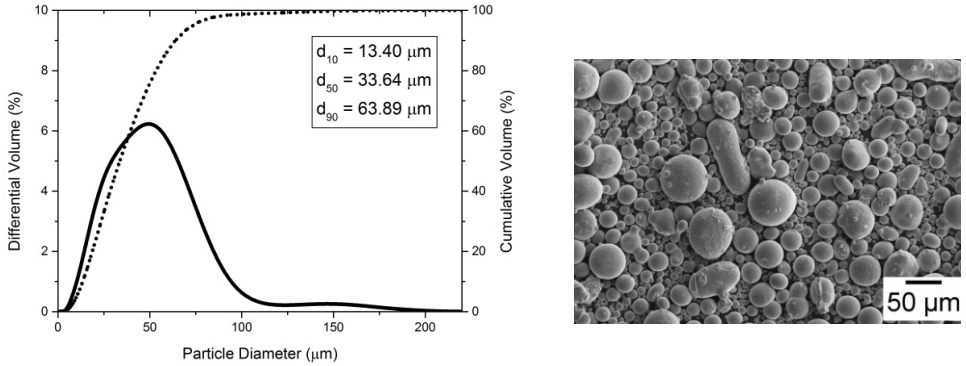

(a) (b)

Figure 18: *Sieved HCWI powder (<63 μm). a) Particles size distribution and b) SEM micrograph of the powder.*

Fig. 19b illustrates particle morphology in the Hadfield steel powder. The particle size distribution of the Hadfield steel powder, shown in Fig. 19a, was positively skewed but less so than in the case of the HCWI. The mean diameter in this case was 39.12 μm. Similarly to the HCWI powder, the particles were mostly spherical.

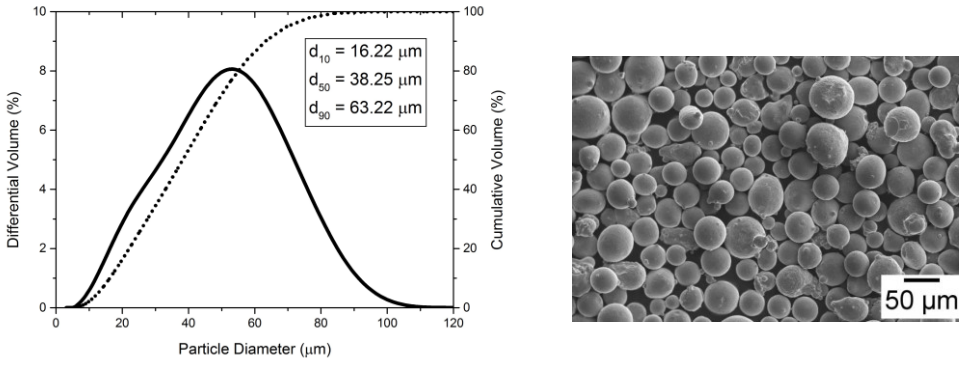

(a) (b)

Figure 19: *Sieved Hadfield steel powder (<63 μm). a) Particle size distribution and b) SEM micrograph of the powder.*

The SEM micrographs of Fig. 20 show typical examples of particles observed in the HCWI and Hadfield steel powders. In both cases, the surface texture appeared to reflect dendritic solidification structure.

The microstructure of the particles, shown in Fig. 21, was dendritic for both the HCWI and Hadfield steel. As the solidification of the droplets was progressing during the solidification, more and more solute atoms were rejected in the last liquid that solidifies. This micro-segregation resulted in the interconnected phase that was clearly visible in the SEM micrographs of Fig. 21.

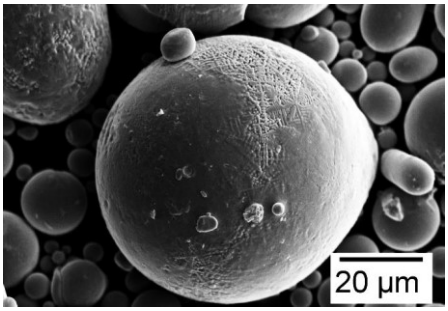

(a) HCWI

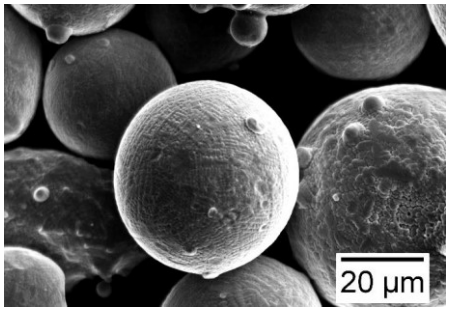

(b) Hadfield steel

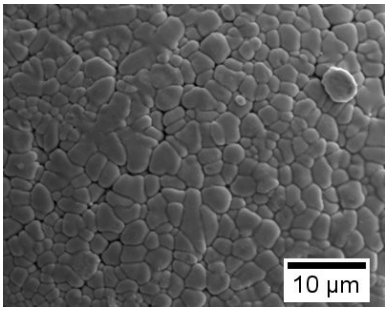

(c) Hadfield Steel

Figure 20: *SEM micrographs illustrating the particles morphology of a) HCWI and b) and c) Hadfield steel.*

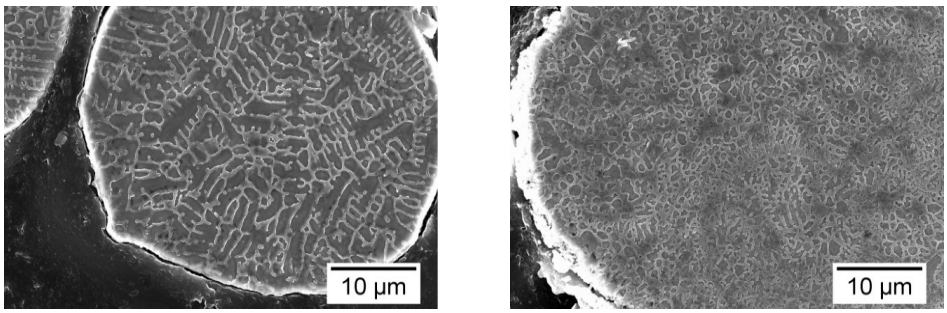

(a) (b)

Figure 21: *SEM micrograph showing the microstructure of the HCWI and Hadfield steel particles.*

6.2 Sintering Behavior

Densification Behavior of High Chromium White Iron

Measured densities of the HCWI samples are listed in Table 7. As expected for set A, the density increased with the sintering temperature. The density of the sample A4 (1050 °C, no dwell time) was lower than that of sample B1 (1050 °C, 5 minutes dwell time), indicating that further densification occurred during the dwell period. The density difference in set B was negligible indicating that 5 minutes of dwell time was already enough to reach the maximum density. The densities of samples in set C were very close to those measured for samples in set B. This indicated that the final density was not significantly influenced by heating rate.

Table 7: *Densities of the samples.*

Set	Process parameters	Density (g/cm^3)
A	900 °C, 0 min, 100 °C/min	5.78 ± 0.06
	950 °C, 0 min, 100 °C/min	6.08 ± 0.02
	1000 °C, 0 min, 100 °C/min	6.76 ± 0.02
	1050 °C, 0 min, 100 °C/min	7.22 ± 0.02
	1100 °C, 0 min, 100 °C/min	7.49 ± 0.02
B	1050 °C, 5 min, 100 °C/min	7.48 ± 0.01
	1050 °C, 10 min, 100 °C/min	7.50 ± 0.01
	1050 °C, 10 min, 100 °C/min	7.50 ± 0.01
C	1050 °C, 10 min, 25 °C/min	7.50 ± 0.01
	1050 °C, 10 min, 400 °C/min	7.50 ± 0.01

Porosity level of samples in set A was determined by image analysis (ImageJ) from BSE images. The determined porosity values are listed in Table 8. The values obtained with Archimedes' method can be compared with these values by assuming a theoretical density of 7.56 g/cm^3. The value for the theoretical density was calculated by using the determined porosity level to extrapolate the measured density value of sample A5 to that of a fully dense material.

Table 8: *Porosity levels in set A determined by image analysis and Archimedes' method.*

Sample ID	Archimedes' method (%)	Image analysis (%)
A1	23.6	27.60
A2	19.6	20.15
A3	10.7	8.29
A4	4.6	4.40
A5	0.96	0.96

The evolution of the particle contacts with increasing temperature for HCWI is illustrated in Fig. 22.

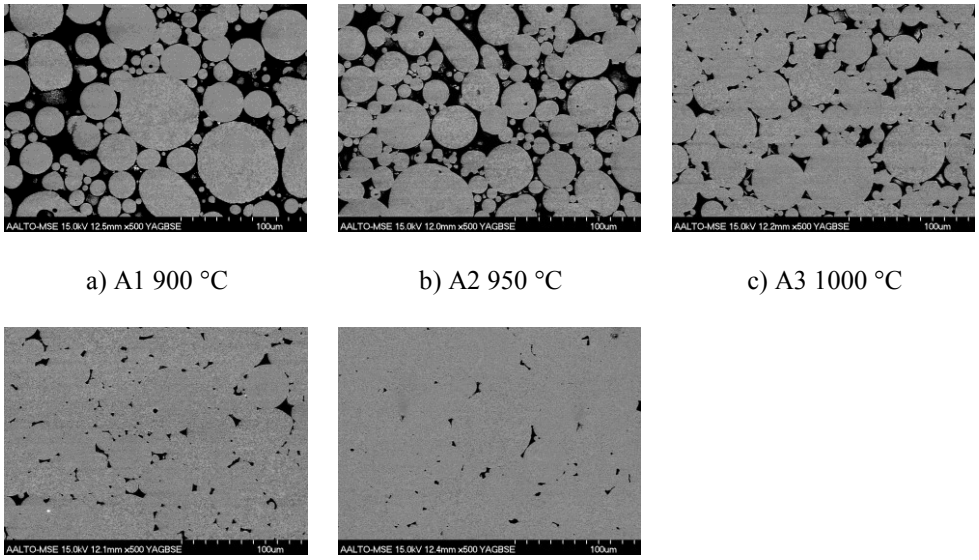

a) A1 900 °C b) A2 950 °C c) A3 1000 °C

d) A4 1050 °C e) A5 1100 °C

Figure 22: *SEM micrographs illustrating densification as a function of sintering temperature (set A).*

The instantaneous density during sintering stage can be roughly estimated by subtracting the contribution of thermal expansion from the relative piston travel. The piston travel resulting from thermal expansion of the graphite mold was determined by carrying out a test compaction without the HCWI

powder. The thermal expansion of the HCWI was calculated by using a literature value of 1×10^{-5} [45] for the coefficient of thermal expansion. The calculations assumed that no diameter change occurs during sintering apart from that of resulting from thermal expansion.

Fig. 23 shows the instantaneous relative density and measured relative density plotted against sintering temperature. The theoretical density was assumed to be 7.56 g/cm^3. There was a clear difference between the measured final density and calculated instantaneous density. The difference was believed to correspond to densification that occurred at the high temperature portion of the cooling segment and the accuracy of the measurement of the displacement rate by the PECS equipment.

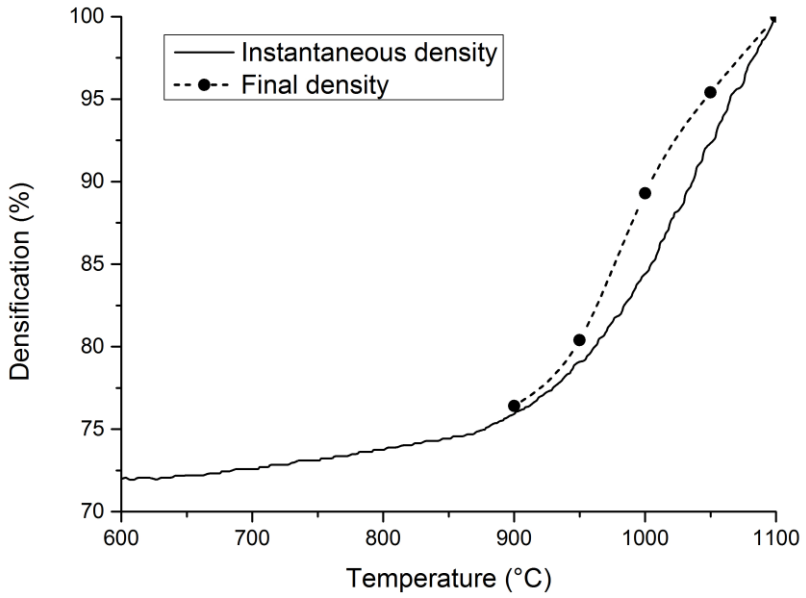

Figure 23: *Evolution of instantaneous and measured density with sintering temperature (no dwell segment; data from set A).*

Density of the Composites

The densities of the composite samples are listed in Table 9. As expected, based on the different mixture ratios, the density of the composite samples varied linearly from sample D0 to sample D100.

Table 9: *Density of the samples in set D.*

Sample ID	Density (g/cm3)
D0 (Hadfield steel)	7.74 ± 0.01
D25 (25 wt% HCWI)	7.66 ± 0.02
D50 (50 wt% HCWI)	7.60 ± 0.02
D75 (75 wt% HCWI)	7.54 ± 0.02
D100 (HCWI)	7.48 ± 0.01

Upper Limit to the Sintering Temperature

In order to establish the maximum temperature for set B, a test compaction was carried out at 1100 °C for 5 minutes. Severe melting occurred during the dwell segment as illustrated in Fig. 24.

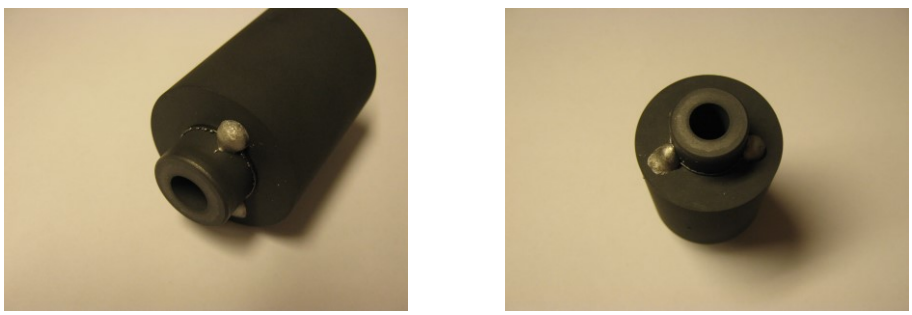

Figure 24: *Mold after a compaction that involved partial melting of the sintered material.*

Because of the melting, the subsequent compactions (set B, set C) used sintering temperature of 1050 °C to prevent melting. In case of the Hadfield steel, slight melting occurred already at 1050 °C. Consequently, a sintering temperature of 1040 °C and 3 minutes of dwell time was chosen for the subsequent compactions of Hadfield steel and the composite samples.

6.3 Properties of the Compacts

6.3.1 Microstructure

Phase Composition

Fig. 25 shows the XRD curves of the HCWI powder and samples in set A. No peaks originating from niobium carbides were present in the XRD curve of the powder and sample A1. However, from sample A2 onward there was a peak that progressively increases in intensity with sintering temperature. This peak was determined to originate from niobium carbides. The peaks originating from M_7C_3-type of carbides were of very low intensity in the powder. The XRD curves of samples in set A, on the other hand, showed several high intensity peaks originating from the M_7C_3-type of carbide. This confirmed that most of the carbide precipitation occurred during the sintering. The XRD curves additionally confirmed that sintering changed matrix phase from primarily austenitic to primarily martensitic. The XRD curves of the samples from set B and set C were nearly identical to each other, indicating that dwell time and heating rate did not have any noticeable effect on the phase composition.

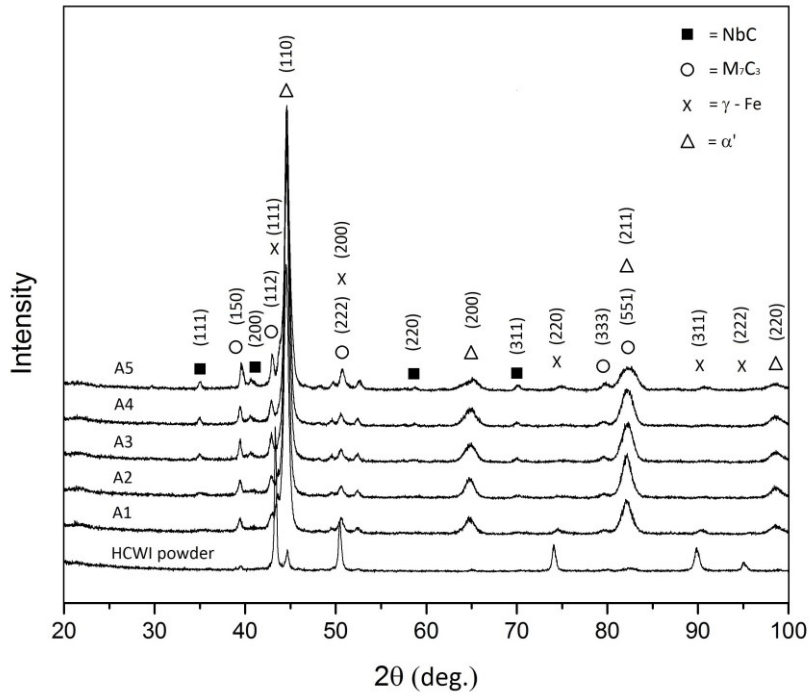

Figure 25: *X-ray diffraction curves of HCWI powder and set A samples.*

Fig. 26 shows the XRD curves of the Hadfield powder and the sample D0. Both curves indicated the presence of austenite. The compacted sample D0 also showed the presence of chromium carbide of type M_7C_3, iron manganese carbide ($Fe_{2.7}Mn_{0.3}C$) and ferrite. The X-ray diffraction curves of the composite samples were the sum of the curves of HCWI and Hadfield steel and they did not reveal any new phases.

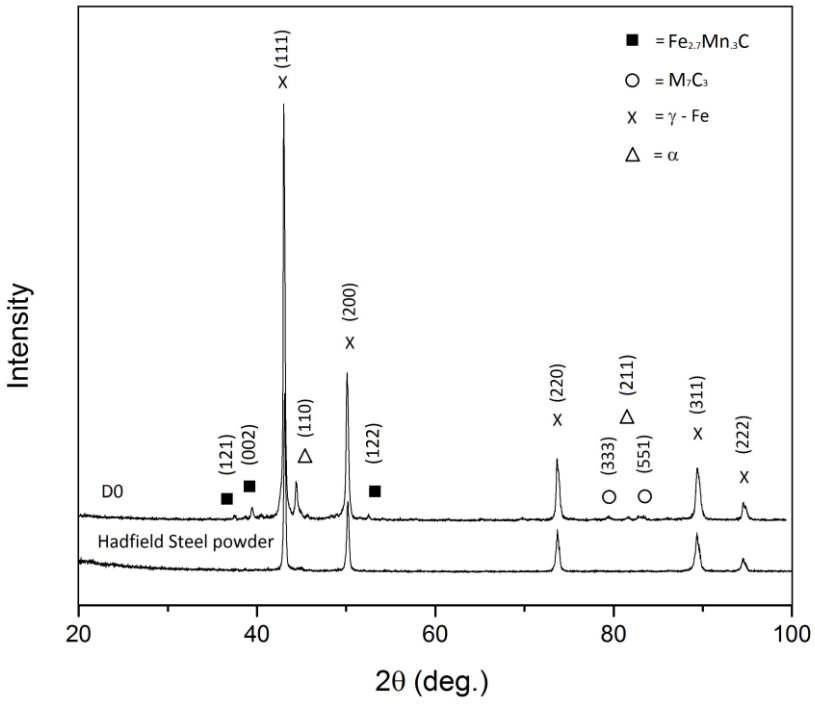

Figure 26: *X-ray diffraction curves of Hadfield steel powder and sample D0.*

Microstructure of the High Chromium White Iron

Fig. 27 shows the evolution of microstructure in the HCWI with increasing sintering temperature. The original dendritic structure of the particle remained visible up to 950 °C. At higher sintering temperature the carbides evolved in a coarser structure, which eventually replaced the dendritic structure.

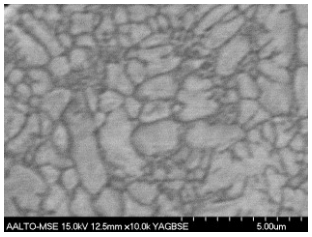

(a) A1 (900 °C)

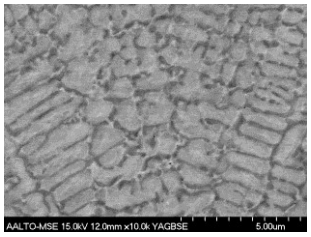

(b) A2 (950 °C)

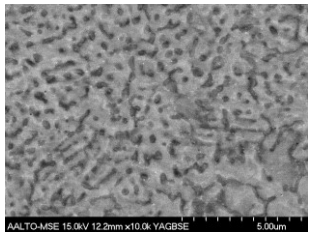

(c) A3 (1000 °C)

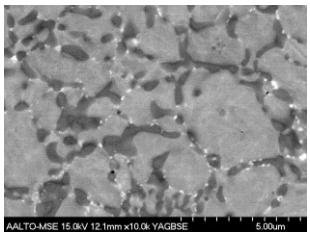

(d) A4 (1050 °C)

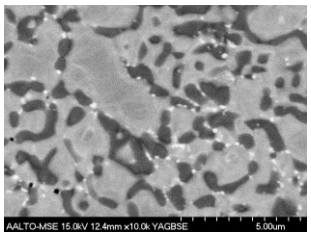

(e) A5 (1100 °C)

Figure 27: *SEM micrograph illustrating evolution of microstructure as a function of sintering temperature (set A).*

The niobium carbides were found preferentially at the carbides-matrix interface. They were visible in the SEM micrographs as bright spots from sample A3 onward (see Fig. 27). Presumably due to limitations in resolving power of the SEM, the niobium carbides could not be observed in the sample A2, even though XRD results clearly indicated their presence. Considerable variation in carbide (M_7C_3) morphology was observed within very close distances, as illustrated in Fig. 28. This was most likely due to orientation differences in particle size and orientation. For instance, areas with very fine carbide morphology most likely corresponded to small particles with a very fine solidification structure.

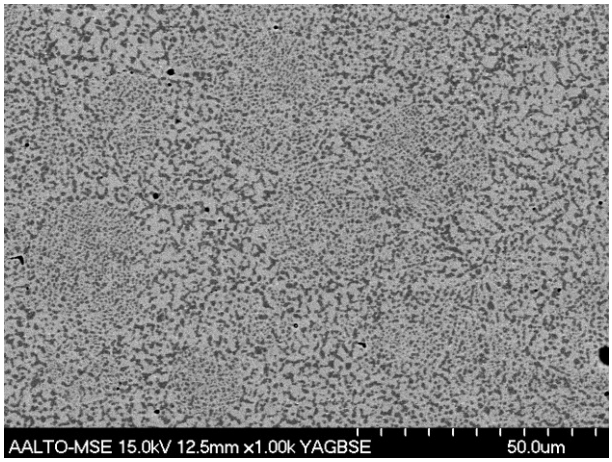

Figure 28: *SEM micrograph illustrating the heterogeneity of the carbides morphology in sample B3.*

The very fine carbide size and heterogeneity of the carbide morphology made it very difficult to carry out a meaningful analysis of carbide morphology. A meaningful analysis would have required covering a much larger surface area using lower magnification. Nevertheless, as illustrated in Fig. 29, qualitative observations indicated that sample B3 had slightly coarser carbide morphology than samples B1 and B2.

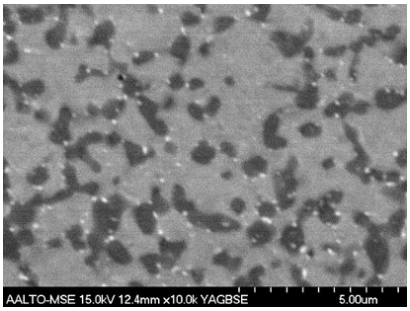

(a) B1

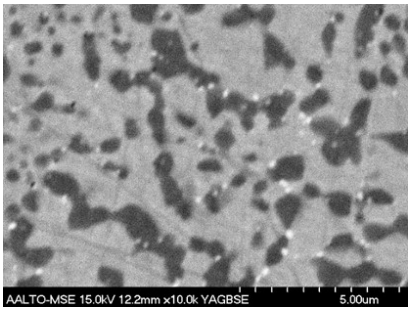

(b) B2

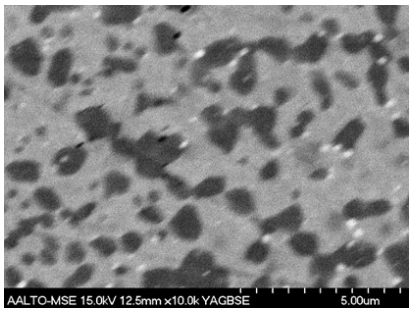

(c) B3

Figure 29: *Evolution of carbide morphology with dwell time (set B).*

Fracture Surfaces

The HCWI samples contained isolated regions (<150 μm) with prior particle boundaries. These were visible on the surface of the polished samples as illustrated in Fig. 30. The prior particle boundaries were not present on the surface of the Hadfield steel sample and composite samples.

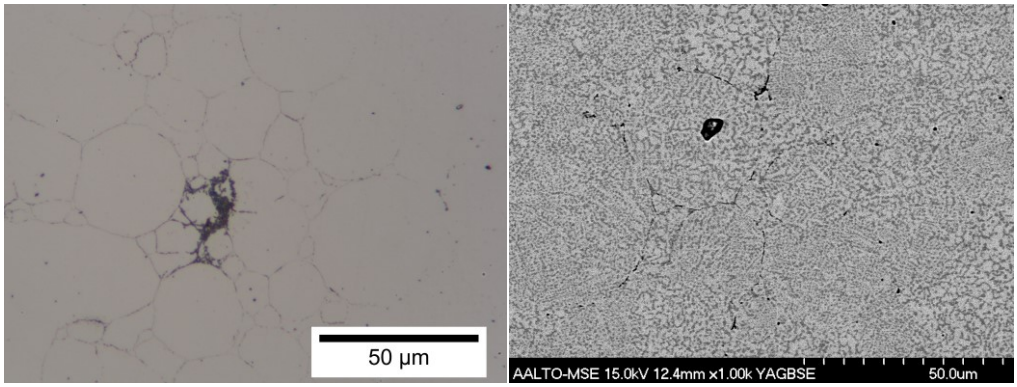

(a) (b)

Figure 30: *a) Optical and b) SEM images of example areas with prior particle boundaries in sample B1.*

The Number of Areas with Prior Particle Boundaries (NAPPB) per unit area was determined using optical microscope. The analyzed surface area covered an area of 20.5 mm^2 per sample. The NAPPB values and the time spent above 850 °C during sintering cycle are listed for selected samples in table 10.

Table 10: *Number of Areas with Prior particle Boundaries (NAPPB) per unit area and time spent above 850 °C for selected samples.*

Sample ID	[NAPPB/ mm^2]	Time [min]
B1	2.10	7
B2	1.76	12
B3	1.17	22
C1	1.90	13
C2	2.93	5.5
Test 1 (10 °C/min)	1.66	25
Test 2 (stop at 500 °C)	2.49	7

As the results in Table 10 indicate, the number of the regions with prior particle boundaries seemed to decrease in frequency with the time spent at high temperature. The presence of prior particle boundaries could be observed in the fracture surfaces as well, as illustrated in Fig. 31. Most of the fracture surfaces, however, showed the typical feature of a ductile fracture with the nucleation of micro-voids around the carbides, as illustrated in Fig. 32.

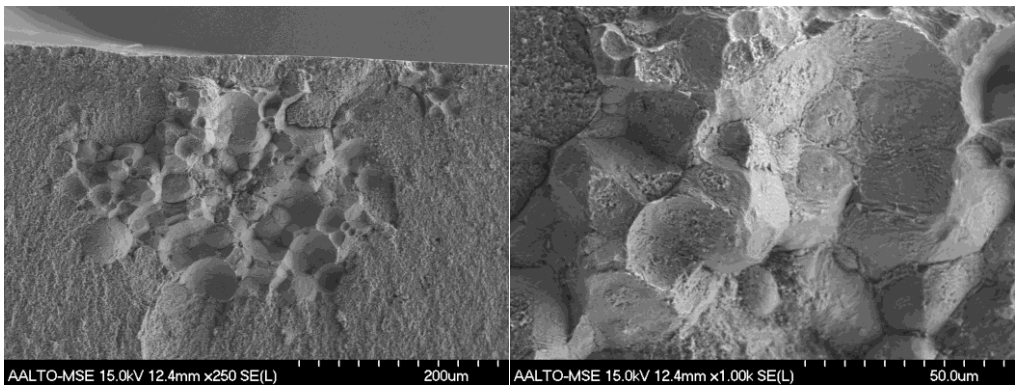

Figure 31: *SEM micrographs of the fracture surface of HCWI illustrating the presence of prior particle boundaries in a test sample.*

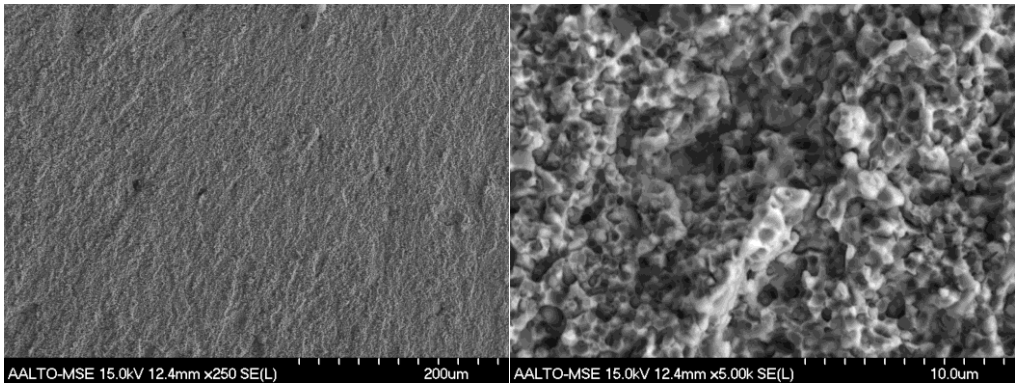

Figure 32: *SEM micrographs showing the fracture surface of a HCWI test sample without the prior particle boundaries.*

Microstructure of the Hadfield steel

Fig. 33 shows the microstructure of the sintered Hadfield steel. The microstructure consisted of ferrous matrix and very fine carbides (~2 μm) homogeneously distributed in the matrix.

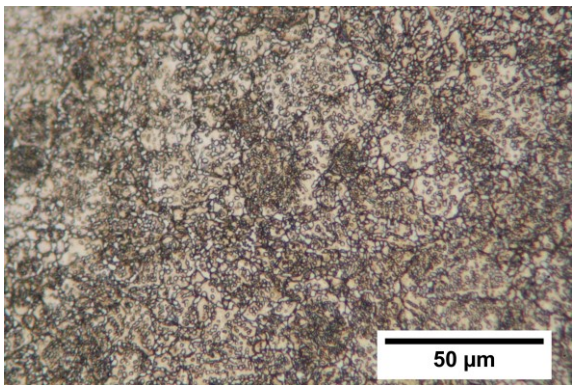

Figure 33: *Optical micrograph showing the microstructure of the sintered Hadfield steel.*

The fracture surface of a Hadfield steel sample, shown in Fig. 34, exhibited ductile fracture mode. Similar to the HCWI, the micro-voids spread from the carbides, eventually leading to fracture of the entire surface.

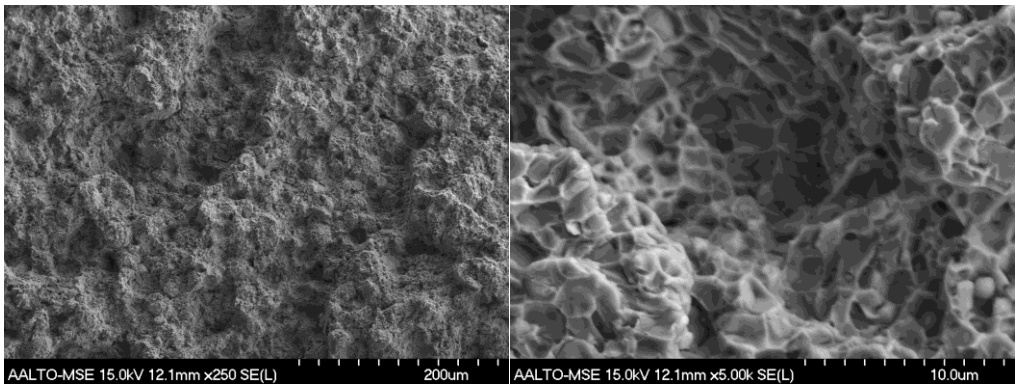

Figure 34: *SEM images showing the fracture surface of a Hadfield steel test sample.*

Microstructure of the Composites

Fig. 35 shows the microstructure of sample D50 (50 wt% HCWI, 50 wt% Hadfield steel). The HCWI had much higher carbide content than the Hadfield steel. Unlike in the HCWI, the grain boundaries were clearly visible in the Hadfield steel.

EDS was used to investigate diffusion across the boundary between HCWI and Hadfield steel in sample D50. The results indicated that manganese is the only element to diffuse to any significant degree between the materials (i.e. diffusion of manganese from Hadfield steel to HCWI).

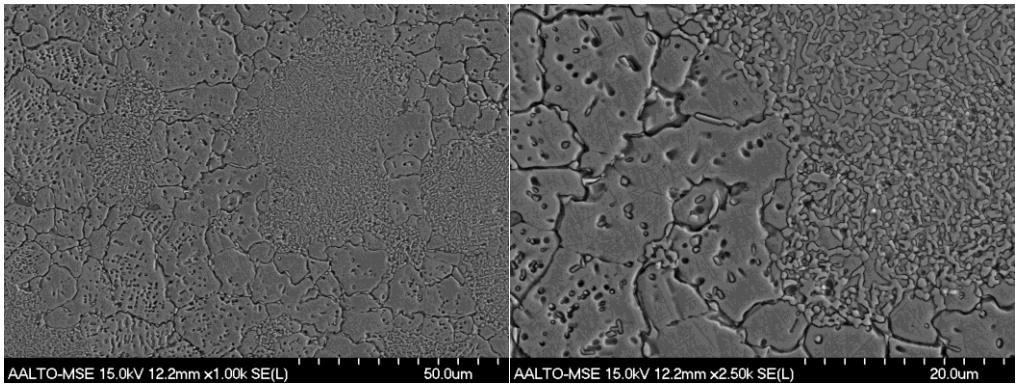

Figure 35: *SEM micrographs illustrating the microstructure of sample D50.The area with more carbides is HCWI (right side), while the area with the grain boundaries is Hadfield steel.*

6.3.2 Hardness

The measured hardness values of the HCWI samples are listed in Table 11.

Table 11: *Measured Rockwell C hardness values of the as-compacted samples.*

Set	Variable	Hardness (HRC)
SET A	1000 °C	47.09 ± 0.27
	1050 °C	57.09 ± 0.19
	1100 °C	62.17 ± 0.14
SET B	5 min	63.24 ± 0.23
	10 min	64.00 ± 0.39
	20 min	64.86 ± 0.43
SET C	25 °C/min	64.17 ± 0.41
	400 °C/min	63.71 ± 0.43
test 1	10 °C/min	65.16 ± 0.37

As can be seen from Table 11, hardness of the HCWI increased with increasing temperature and dwell time. A decrease in the heating rate resulted in higher hardness as well.

The measured hardness values of the composite samples are listed in Table 12.

Table 12: *Measured Rockwell C hardness values of samples in set D.*

Sample ID	Hardness (HRC)
D0	39.41 ± 0.29
D25	42.60 ± 0.35
D50	47.58 ± 0.74
D75	57.89 ± 0.27
D100	63.24 ± 0.26

Fig. 36 shows the hardness values of the composite samples plotted against the HCWI content. As can be seen, the rate at which hardness increase appeared to accelerate as the HCWI content exceeds 50 wt%.

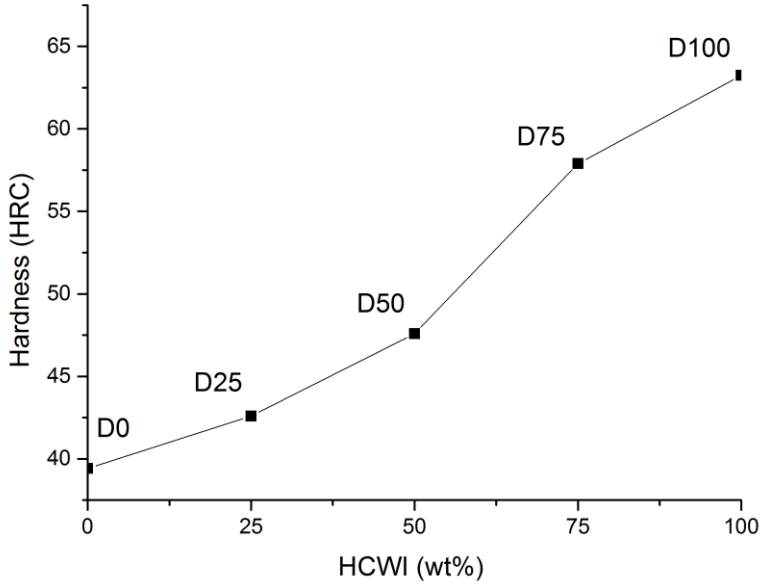

Figure 36: *The measured hardness as a function of the HCWI content (wt%) in the composite samples.*

6.3.3 Abrasion Resistance

Fig. 37a shows the total weight loss experienced by each sample during abrasion testing. The HCWI sample experienced the lowest weight loss (i.e. best abrasion resistance). It was closely followed by the Hadfield steel sample. The composite samples were very similar to each other in weight loss. The weight loss was approximately 20 % higher than of the HCWI and Hadfield steel samples.

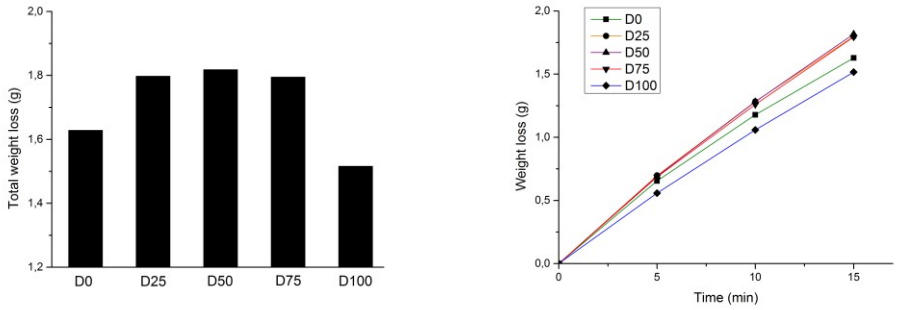

(a) (b)

Figure 37: *a) Total weight loss observed during the abrasion test for set D. b) Weight loss as a function of the testing time.*

The SEM micrographs in Fig. 38 show typical examples of the wear tracks observed on the surfaces of the wear samples (see Appendix for complete sets of micrographs). SEM study of the wear tracks indicated that material was primarily removed by ploughing and cutting. In the micrographs it was possible to identify the groove caused by the sliding sand particles and the material plastically displaced on the side of the groove. The fine carbides were well attached to the ferrous matrix and did not exhibit cracks after the tests.

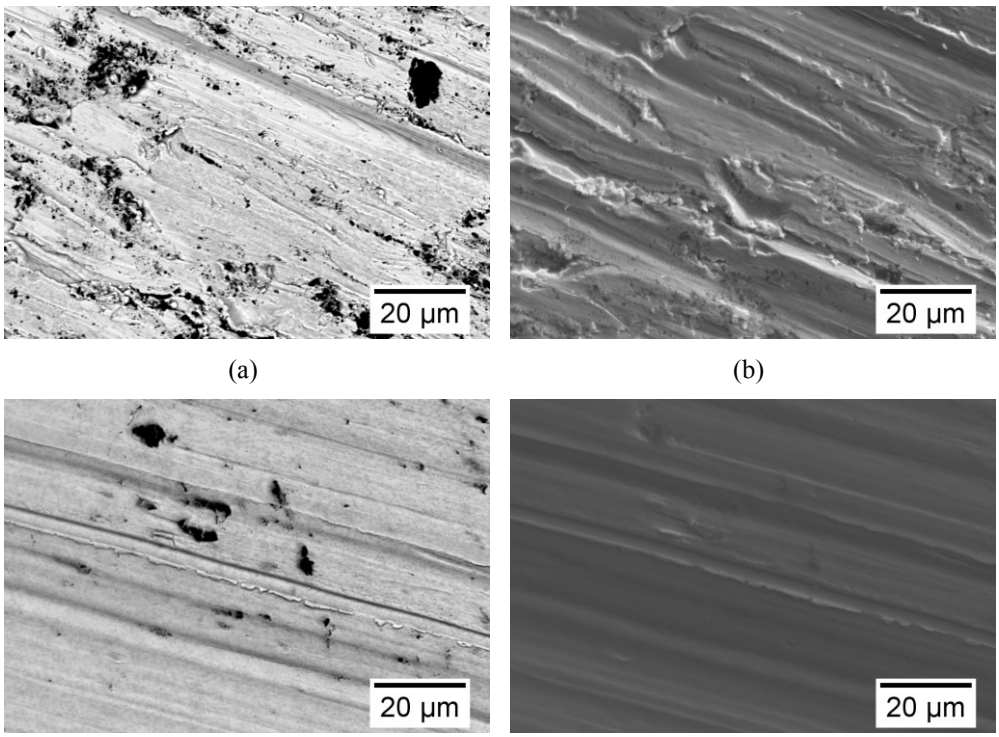

Figure 38: *BSE micrographs of a) D25, c) D100 and SE micrographs of b) D25 d) D100 illustrating the worn surface.*

The BSE micrographs (see Fig. 38a and 38c) revealed presence of dark spots on the wear surfaces. Fig. 39 shows the results from EDS analysis of sample D50. As can be seen, overwhelming majority of the dark spots was concentrated on the manganese rich part of the wear surface. In addition, the locally increased silicon content clearly corresponded to the dark spots on the wear surfaces. This indicated that the dark spots were silica embedded on the wear surface during the wear testing. The fact that there was more silica embedded on the Hadfield steel was not surprising considering that it was much softer than the HCWI.

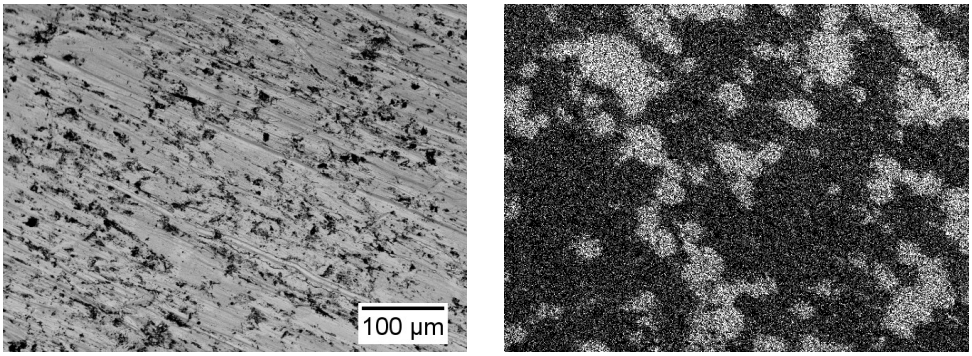

(a) (b) Chromium

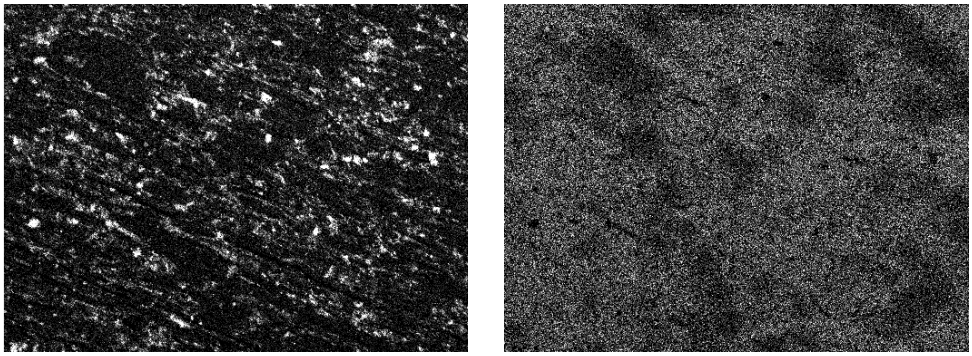

(c) Silicon (d) Manganese

Figure 39: *Results from EDS mapping for sample D50.*

7 Discussion

7.1 Sintering Behavior and Microstructure of the Alloys

The microstructure of the PECS processed HCWI consisted of chromium and niobium carbides in a steel matrix of martensite and some retained austenite. The chromium carbides (<3 μm) were substantially finer than those reported for conventionally cast HCWI (25 μm) [3].

The densification of HCWI was strongly influenced by both the time and temperature. Melting limited the maximum sintering temperature of the HCWI to 1050 °C. The densities obtained at this temperature were the same regardless of the dwell time (5, 10, and 20 min), indicating that no further densification occurs after a dwell period of 5 minutes. Furthermore, the size of the chromium carbide particles was independent of the dwell time. The sintering cycle data indicated that densification started at around 860 °C. This was supported by the early stage of sintering observed in sample sintered at 900 °C without dwell segment (see Fig. 23).

The heating rate had no effect on the carbide size or on the final density of the samples to any significant degree. However, changes to dwell time and heating rate had a slight effect on the hardness of the HCWI. The obtained hardness increased with longer dwell period and higher sintering temperature.

The niobium carbides in the samples were concentrated on the carbide-matrix interface. Their size was usually less than 200 nm. This is significantly finer than the 10 μm reported for niobium carbides in conventionally cast HCWI [8, 47].

Sintering of Hadfield steel was limited to a temperature of 1040 °C since melting occurred above this temperature. The dwell time necessary to reach full density was 3 minutes. The results showed that PECS process is feasible

for the production of Hadfield steel and its microstructure consists in fine carbides (~2 μm) and small grain size (20 μm).

7.2 Abrasion Performance of the Alloys

Hadfield steel was sintered using PECS at 1040 °C and with 3 minutes of dwell time. Hadfield steel had similar processing conditions as HCWI and this allowed the mixing of the two materials to investigate an improvement in abrasion resistance behavior.

The abrasive wear performance of the composite samples, with hardness between the HCWI and Hadfield steel, was lower than the performances of the HCWI and Hadfield steel. The Hadfield steel with lowest hardness of all the materials performed almost as well as the HWCI, which had the highest hardness. In addition, the wear resistance of HCWI was not likely to be influenced by niobium carbides since the size was too small. Clearly, hardness alone was inadequate indicator of abrasive performance.

The similar weight loss between high chromium white iron and Hadfield steel can be explained by the higher toughness and the possibility of work hardening of Hadfield steel. According to the literature, in the case of pin on disk test, Hadfield steel and HCWI showed similar wear resistance when a low load was applied. However, at high loads HCWI performed better than the Hadfield steel [46]. Therefore it is possible that with higher loads in the abrasion test, the HCWI would show significantly higher wear resistance than Hadfield steel.

The higher weight loss of the composite samples can be explained by considering that harder HCWI inhibited Hadfield steel's ability to work harden. This would also explain why the composite samples with 50% of HCWI exhibited the highest weight loss among the composite samples.

8 Conclusions

The present study shows that PECS is capable of processing gas atomized HCWI powder into dense material with fine and uniform carbide morphology. The HCWI samples were obtained at 1050 °C within 5 minutes of dwell time employing a heating rate of 100 °C/min. Composites with different percentages of HCWI and Hadfield were pulsed electric current sintered at 1040 °C and 3 minutes of dwell time.

The microstructural studies of HCWI revealed that the carbide structure was only slightly influenced by the changes in processing parameters, such as dwell time and heating rate. The niobium carbides precipitated during sintering were concentrated preferentially at the chromium carbide-matrix interface and exhibited a very small size in the order of 200 nm.

The abrasion tests revealed that mixing HCWI with Hadfield steel does not improve the abrasion resistance. HCWI had the highest wear resistance followed by Hadfield steel, while the three composite samples (25%, 50% and 75% of HCWI) exhibited higher weight loss (~20%) than both HCWI and Hadfield steel. This was even though they had higher hardness than the Hadfield steel.

The results indicate that significant modification of carbide morphology of HCWI is not feasible via modification of process parameters in PECS. The results furthermore show that abrasion resistance of HCWI is not favorably influenced by mixing it with Hadfield steel. Future research should evaluate how the composite samples behave under impact type of wear environment with respect to HCWI and Hadfield steel. These studies might answer whether the fine carbide structure or mixing of the HCWI with tougher material (e.g. Hadfield steel) provides better toughness, and consequently better wear performance in impact type of wear conditions.

References

1. Sahoo P., *"Engineering Tribology"*, New Dehli, Asokek Ghosh Prentice-Hall of India Private Limited, 2005.

2. Stachoviak G., *"Engineering Tribology (3rd Edition)"*, Butterworth-Heinemann.

3. Tabrett C. P., Sare I. R., Ghomashchi M. R., "*Microstructure-Property Relationships in High Chromium White Iron Alloys*", International Materials Reviews 1996 Vol. 41 No.2.

4. Dogan O.N., Hawk J.A., Laird G., "*Solidification Structure and Abrasion Resistance of High Chromium White Irons*", Metallurgical and Materials Transactions Vol. 28A, JUNE 1997–1315.

5. Scandian C., Boher C., De Mello J.D.B., Rézaï-Aria F., "*Effect of Molybdenum and Chromium Contents in Sliding Wear of High-Chromium White Cast Iron: The Relationship Between Microstructure and Wear*", Wear 267 (2009) 401–408.

6. Bramfitt B. L., Arlan B. O., *"Metallographer's Guide - Practices and Procedures for Irons and Steels"*, ASM International, 2002.

7. Krauss G., *"Steels Heat Treatment and Processing Principles"*, ASM International, 1990.

8. Filipovic M., Kamberovic Z., Korac M., Gavrilovski M., *"Microstructure and Mechanical Properties of Fe–Cr–C–Nb White Cast Irons"*, Materials and Design 47 (2013) 41–48.

9. Kennedy R., Krauss G., Roberts G., "*Tool Steels"*, ASM International, 1998.

10. Coronado J.J., Sinatora A., *"Abrasive Wear Study of White Cast Iron with Different Solidification Rates"*, Wear 267 (2009) 2116–2121.

11. Davis J. R., *"Cast Irons"*, ASM International, 1996.

12. Bhushan B., "*Introduction to Tribology"*, New York, John Wiley and Sons, 2002.

13. Cemil C., *"An Investigation of the Wear Behaviours of White Cast Irons under Different Compositions"*, Materials and Design 27 (2006) 437–445.

14. Reda R., Nofal A., Ibrahim Kh., Hussien A., *"Investigation of Improving Wear Performance of Hypereutectic 15%Cr-2%Mo White Irons"*, The 69th WFC Paper Vol. 7 No. 4.

15. Hanlon D.N., Rainforth W.M., Sellars C.M., *"The Rolling Sliding Wear Response of Conventionally Processed and Spray Formed High Chromium Content Cast Iron at Ambient and Elevated Temperature"*, Wear 225–229 (1999) 587–599.

16. ASM International Handbook Committee (ed.), *"ASM Metals HandBook Volume 1 – Properties and Selection: Irons, Steels, and High Performance Alloys"*, ASM International, 1990.

17. Dogan O.N., Hawk J.A., *"Effect of Carbide Orientation on Abrasion of High Cr White Cast Iron"*, Wear 189 (1995) 136–142.

18. Callister W. D., Rethwisch D. G., *"Materials Science and Engineering an Introduction"*, John Wiley and Sons, 2009.

19. Tanga X.H., Chunga R., Li D.Y., Hinckleyb B., Dolmanb K., "*Variations in Microstructure of High Chromium Cast Irons and Resultant Changes in Resistance to Wear, Corrosion and Corrosive Wear*", Wear 267 (2009) 116–121.

20. Carpenter S.D., Carpenter D., Pearce J.T.H. , *"XRD and Electron Microscope Study of an As-cast 26.6% Chromium White Iron Microstructure"*, Materials Chemistry and Physics 85 (2004) 32–40.

21. http://www.acmealloys.com/Austenitic%20Manganese%20Steels.PDF , 28.04.2014

22. http://steel.keytometals.com/Articles/Art69.htm, 28.04.2014

23. Yan W, Fang L, Sun K, "*Effect of Surface Work Hardening on Wear Behavior of Hadfield Steel*" Materials Science and Engineering, 2007, 460–461.

24. Bouaziz O., Allain S., Scott C.P., Cugy P., Barbier D., "*High Manganese Austenitic Twinning Induced Plasticity Steels: A Review of the Microstructure Properties Relationships*", Current Opinion in Solid State and Materials Science 15 (2011) 141–168.

25. Raynor G.V., Rivlin V.G., "*Phase Equilibria in Iron Ternary Alloys: A Critical Assessment of the Experimental Literature*", The Institute of Metals I Carlton House Terrace, London, 1998

26. Hryha E., "*Critical Aspects of Alloying of Sintered Steels with Manganese*", Metallurgical and Materials Transactions A 41A (2010) 2880–2897.

27. Schroeder R., Binder C., Klein A. N., "*Sinterability and Microstructure Formation of a Hadfield Steel Produced by MIM*", Materials Laboratory (LabMat), Federal University of Santa Catarina, Florianopolis, Brazil. Whirlpool / Embraco unit. Joinville, Brazil.

28. Kang S.-J. L., "*Sintering: Densification, Grain Growth, and Microstructure"*, Jordan Hill, GBR, Butterworth-Heinemann, 2005.

29. German R. M., "*Sintering Theory and Practice"*, New York, United States, John Wiley and Sons, Inc., 1996.

30. German R. M., "*Powder Metallurgy of Iron and Steel"*, Wiley and Sons, Inc., 1998.

31. ASM International Handbook Committee (ed.*),"ASM Handbook Volume 7 – Powder Metal Technologies and Applications"*, ASM International, 1998.

32. Grasso S., Sakka Y., Maizza G., "*Electric current activated/assisted sintering (ECAS): a review of patents 1906–2008*", Science and Technology of Advanced Materials 10 (2009).

33. Munir Z. A., Quach D. V., *"Electric Current Activation of Sintering: A Review of the Pulsed Electric Current Sintering Process"*, Journal of the American Ceramic Society Munir et al. Vol. 94, No. 1

34. Anselmi-Tamburini U., Gennari S., Garay J.E., Munir Z.A., "*Fundamental investigations on the spark plasma sintering/synthesis process II. Modeling of current and temperature distributions*", Materials Science and Engineering A 394 (2005) 139–148.

35. Tokita M., *"Mechanism of Spark Plasma Sintering"*, Sumitomo Coal Mlmng Company, Ltd.

36. Chen W., Anselmi-Tamburini U., Garay J.E., Groza J.R., Munir Z.A., "*Fundamental investigations on the spark plasma sintering/synthesis process I. Effect of dc pulsing on reactivity*", Materials Science and Engineering A 394 (2005) 132–138.

37. Omori, M., "*Sintering, consolidation, reaction and crystal growth by the spark plasma system (SPS)*," Materials Science and Engineering A287 (2000) 183–188.

38. Munir Z.A, Anselmi-Tamburini U., Ohyanagi M., "*The effect of electric field and pressure on the synthesis and consolidation of materials: A review of the spark plasma sintering method*", Journal of Material Science, vol.41, no. 3, pp. 763–777, 2006.

39. Orrù R., Licheri R., Locci A. M., Cincotti A., Cao G., "*Consolidation/synthesis of materials by electric current activated/assisted sintering*", Materials Science and Engineering: Reports Vol. 63, Issues 4–6, 12 February 2009, Pages 127–287.

40. Yucheng W., Zhengyi F., "*Study of temperature field in spark plasma sintering*", Materials Science and Engineering B90 (2002) 34–37.

41. Hulbert D. M., Anders A., Andersson J., Lavernia E. J., Mukherjee A. K., "*A discussion on the absence of plasma in spark plasma sintering*", Scripta Materialia 60 (2009) 835–838.

42. http://www.fct-systeme.de/en/content/Spark_Plasma_Sinteranlage_Typ_HPD_HHPD/~nm.12~nc.32/Spark-Plasma-Sinteranlage-Typ-HP-D--HHP-D.html#x, 28.04.2014.

43. Sartorius YDK 01, YDK 01-0D, YDK 01 LP, User's Manual

44. ASTM Standard G65, *"Standard Test Method for Measuring Abrasion Using the Dry Sand/Rubber Wheel Apparatus"*, ASTM International, West Conshohocken, PA.

45. ASM Ready Reference: Thermal properties of metals, ASM International, 2002

46. Atabaki M. M., Jafari S., Abdollah-pour H., *"Abrasive Wear Behavior of High Chromium Cast Iron and Hadfield Steel-A Comparison"*, Journal of Iron and Steel Research, International. 2012.

47. Zhi X., Xing J., Fu H., Xiao B., *"Effect of Niobium on the As-cast Microstructure of Hypereutectic High Chromium Cast Iron"*, Materials Letters 62 (2008) 857–860.

Appendix: SEM Micrographs of the Wear Surfaces

Back-scattered electron micrographs (left side) and secondary electron micrographs (right side) illustrating the worn surface of composite samples.

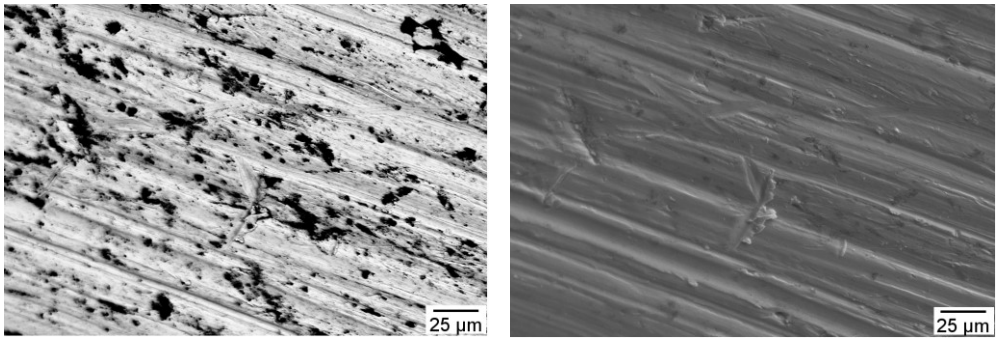

Sample D0.

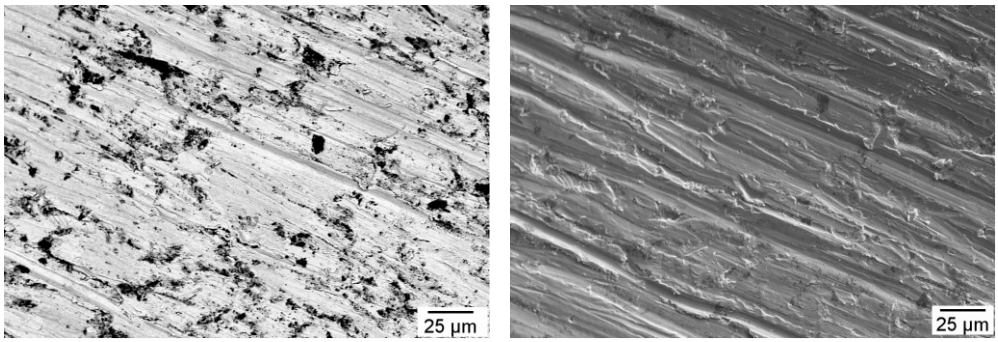

Sample D25.

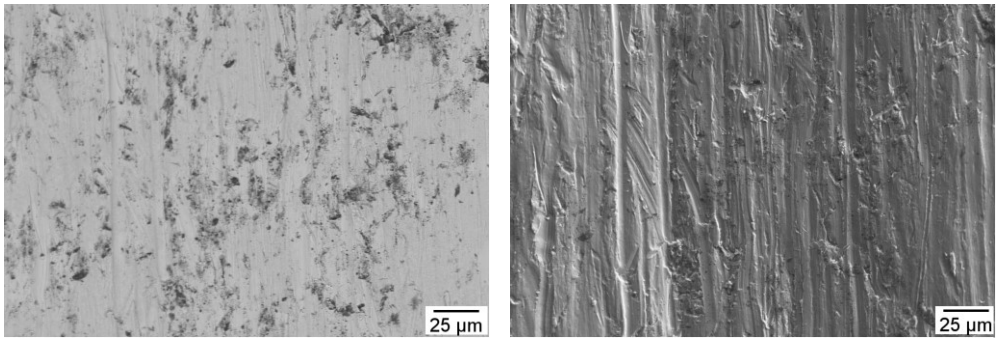

Sample D50.

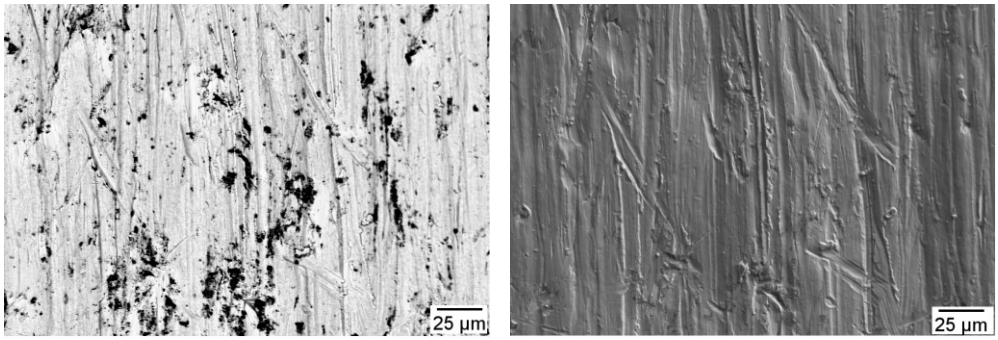

Sample D75.

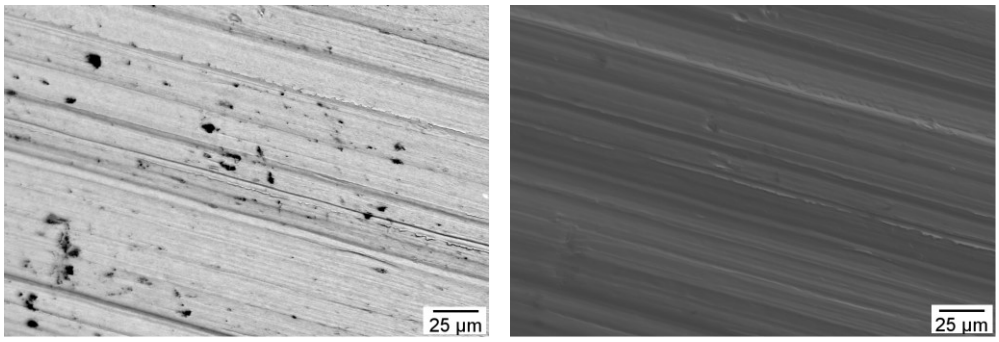

Sample D100.